Nanoparticle-Supported, Rapid, and Electronic Detection of SARS-CoV-2 Antibodies and Antigens at Attomolar Level

Yeji Choi[1,2 #], Seyedsina Mirjalili[1,2 #], MD Ashif Ikbal[1,2], Sean McClure[1], Scott Clemens[1], Jose Solano[1], John Heggland[1], Jiawei Zuo[1], and Chao Wang[1,2]*

[1]School of Electrical, Computer and Energy Engineering, Arizona State University, Tempe, AZ 85287, USA

[2]Biodesign Center for Molecular Design and Biomimetics, Arizona State University, Tempe, AZ 85287, USA

#Equal Contributions:

1- Yeji Choi

2- Seyedsina Mirjalili

***Corresponding Author: wangch@asu.edu**

Keywords

SARS-CoV-2; Gold nanoparticles; Point of care; Rapid electronic detection; Antibody detection; Rapid antigen detection

Abstract

A gold nanoparticle (AuNP)-supported rapid, electronic detection (NasRED) platform is demonstrated with high specificity to differentiate SARS-CoV-2 from human coronaviruses while achieving high sensitivity. Uniquely, active fluidic force is exerted on AuNPs in a microcentrifuge tube, through engineered centrifugation and vortex agitation, to accelerate signal transduction from biochemical protein binding to physical AuNP aggregation and precipitation and finally to electronic signals in a customized, stabilized circuitry. The limits of detection are found <80 aM (12 fg/mL) and ~700 aM (105 fg/mL) to detect antibodies in human pooled serum and 20% diluted whole blood, and <900 aM (45 fg/mL) and 4.1 fM (200 fg/mL) to detect nucleocapsid proteins in human saliva and nasal fluid, respectively. With a small test volume (6 µL), a rapid turnaround time (as fast as <15 min), low reagent cost (estimated ~$2), and a small system footprint, this novel digital platform can be utilized for accurate diagnosis and screening of a wide range of infectious and chronic diseases.

Introduction

Infectious diseases pose a serious threat to human health and the world economy. For example, COVID-19 alone has caused more than 775 million infections and 7 million deaths as of May 5th, 2024[1], and an estimated $14 trillion in economic losses to the U.S. by the end of 2023[2]. In addition, the pandemic also seriously strained the global healthcare system[3,4] and caused delayed or missed diagnosis or treatment to many other patients. To better prepare for future pandemics, which could be caused by a currently unknown disease 'X'[5,6], it is of paramount importance to continue to invest in new diagnostic technologies that can accurately detect and quantify diseases early in a portable, inexpensive, and easy-to-operate fashion so that the tests can be accessible to all patients in need, including those from rural areas and low- to middle-income countries, where medical resources are scarce.

Conventionally, molecular and immunochemical tests are typically used to diagnose infectious diseases, including COVID-19[7,8]. These tests look for molecules of different genetic information to diagnose diseases and predict the risk of unknown diseases[9]. Nucleic Acid Amplification Tests (NAATs), including Polymerase Chain Reaction (PCR) and Loop-mediated Isothermal Amplification (LAMP), leverage the feasibility of DNA or RNA amplification to maximize the sensitivity. However, as the gold standard of lab tests, PCR requires hours to days to amplify and confirm the results due to the multiple steps of sample handling and the thermal cycling process[10]. Additionally, it requires expensive and large equipment, and is more suited for centralized detection but not accessible in resource-limited settings. Isothermal amplification methods such as LAMP, as an alternative to PCR, require much cheaper instruments; however, the sensitivity heavily depends on the primer design, which constrains target site selection and assay specificity.

Immunochemical tests diagnose diseases by confirming the presence or absence of a specific protein based on antigen-antibody reactions. The diagnosis is mainly performed by Enzyme-Linked Immunosorbent Assay (ELISA) and Lateral Flow Assay (LFA)[11]. ELISA typically has a sensitivity of picomolar concentration from biological fluids [12–14]. However, like PCR, ELISA is most suited for high-sensitivity analysis of large amounts of samples in laboratory settings since it requires a multistep and complex workflow, making it highly labor-intensive and expensive[15,16]. In addition, Rapid Antigen Tests (RATs) such as LFA are portable for field applications but typically have lower sensitivity (e.g., 65.3% for COVID-19), thus not ideal for accurate detection, particularly at early-stage infection when the viral load is low[17–19].

Here, using SARS-CoV-2 as an example, we report a prototyped, inexpensive, miniaturized sensing system, i.e. nanoparticle-supported rapid electronic detection (NasRED), to detect the antibodies and antigens directly from serum, whole blood, saliva, and nasal fluid within a short time (15 to 30 min, comparable to LFA) and achieve high sensitivity (attomolar, or fg/mL, about 2 to 3 orders better than ELISA[20] and about 4 to 5 orders of magnitude better than LFA[21]), enabling rapid and accurate diagnostics of infectious diseases that can be accessed in different clinical settings. Specifically, our digital sensing platform was designed to detect the target proteins by simply mixing bodily fluids with our prepared sensing solution comprising functionalized gold nanoparticles (AuNPs) in a testing tube [22,23]. The mixing, reaction, and readout were all completed in the same tube without washing, labeling, or fluorescent imaging, thus greatly reducing operation complexity. The sensing signals were collected, digitized, and transmitted using our customized semiconductor devices and circuits, which also minimized signal fluctuations to enable accurate detection of antigens and antibodies at ultralow concentrations. Further, we comprehensively optimized the sensing protocol, i.e. the centrifugation and vortex agitation speed and time, to

greatly improve the limits of detection (LoDs) of SARS-CoV-2 antibody (AS35) and antigen (N-protein) to ~<0.1 pg/mL from a wide range of bodily fluids, including in 20% diluted whole blood without plasma separation. Lastly, using inactivated SARS-CoV-2 virion particles, NasRED proved successful in detecting 422 aM (21 fg/mL) N-protein and achieving an estimated RNA sensitivity of 33 copies/mL, outperforming conventional ELISA and PCR. Together, our preliminary daa suggests a great promise of NasRED as a new and broadly applicable platform for highly sensitive, rapid, and accessible detection of infectious diseases as well as chronic diseases.

Results

NasRED sensing platform

The NasRED protein sensing platform can be applied to the detection of both the antigens and the antibodies (Figure 1). The sensors are prepared by attaching biotinylated proteins to streptavidin-coated AuNPs using a biotin-streptavidin reaction, where the protein binders can be antigens (e.g. SARS-CoV-2 spike (S) or receptor binding domain (RBD) proteins) for antibody (neutralizing antibody AS35) sensing or antibodies (mAbs AS47 and AM223) for antigen (nucleocapsid (N) protein) sensing (Figure 1a). Using antibody sensing as an example (Figure 1b), 18 µL of the RBD-functionalized AuNPs were mixed with 6µL of medium (e.g., PBS buffer, human pooled serum (HPS), and human whole blood (WB)) containing target SARS-CoV-2 antibodies diluted to desired concentrations. A sample of blank medium without antibodies was used as a negative control (NC). For rapid detection, the 24 µL mixture was centrifuged at 1,200 g for 5 minutes and incubated for 5 minutes to precipitate the functionalized AuNPs to the bottom of the microcentrifuge tube, where their concentration was greatly enhanced. Such a localized and boosted reactant concentration significantly promoted the localized reaction with target proteins,

thus accelerating the antibody-antigen reaction at low concentrations to achieve an ideal LoD and reduced assay time. To preserve the detection specificity, a vortex agitation was introduced to disperse unbound AuNPs without disturbing the precipitated AuNP clusters, verified by fully dispersed AuNPs in the NC reference. The optical absorption signal from the supernatant, resulting from free-floating AuNPs after vortexing, was digitized using a portable electronic detector (PED) for quantification (Figure 1d). The electronic signals of the antigen or antibody samples collected from the PED represented the optical transmission of LED light through the supernatant in the microcentrifuge tube and were normalized (Methods). The NasRED system has proven to be feasible to detect antigens and antibodies from complex biological fluids at high sensitivity and high specificity (Figure 1f-g).

Signal-stabilizing circuit for low-noise detection

The NasRED platform consisted of a portable electronic detector (PED) for signal readout that had two customized parts (Figure S1). The first part was a semiconductor-based, digital, signal-collecting device made of a light-emitting diode (LED), a photodetector (PD), and a microcentrifuge tube chamber to block ambient light. This device functioned to probe the free-floating AuNP concentration in the supernatant of the testing tube and to digitize the optical signals of the AuNPs to electronic current signals. The second part was a circuit board that stabilized the LED and PD signals for reliable antibody or antigen detection. Electronically, the stabilizing circuit board (Figure 2a-b, Figure S2) had three key components: a voltage regulator to adjust the power supply input to the desired value for the LED circuit and microprocessor, a constant current LED driver circuit to stabilize the light intensity, and a microprocessor for signal processing. The regulator circuit comprised two electrolytic capacitors, two ceramic capacitors, and one protective

Zener diode (Figure 2a (i)). The constant current LED driver circuit utilized a feedback loop that coordinated double bipolar junction transistors (BJTs, T1 and T2 in Figure 2a (ii)) to stabilize the current supplied to the LED. In addition, we further customized a microprocessor (Figure 2a (iii)) to process the signals and communicate with laptops through USB, Wi-Fi, or Bluetooth modules. Without the stabilization circuit, the LED displayed a large deviation in current (average 0.14 mA over 10 minutes but significantly increased after 40-min operation, possibly due to heating, Figure 2c), and the PED produced random spike noises when used to test AS35 antibodies in PBS (Figure 2d). This could be understood from the fact that the LED light emission is proportional to its electrical current and exponentially depends on the bias voltage, and therefore, a slight voltage fluctuation from a power glitch or device heating could produce a systematic error that eventually seriously limits the sensing performance at low analyte concentrations. In comparison, our improved readout system demonstrated significantly reduced current fluctuation (0.12 mA within the first two minutes during circuit initiation and decreased to 0.02 mA during the rest 60-min testing period, Figure 2c) and greatly minimized system error in antibody detection (Figure 2d), indicating significantly higher stability.

Impacts of centrifugation and vortex agitation on sensing performance

The centrifugation and vortex agitation actively modulate the reagent and AuNP distribution in the buffer solutions, thus providing additional degrees of freedom to optimize the sensitivity and specificity. To examine their impacts on the NasRED assay performance, we chose mAb AS35 (6 µL, from 4 µM to 40 fM in PBS) as the target antibody using AuNPs functionalized with WT-RBD (Wuhan-Hu-1, 18 µL in1×PBS dilution buffer), and collected the electronic signals using our stabilized readout system. Here, a series of tests (Figure 3) were performed by changing four

variables: the centrifugal force gravity (g) (Figure 3a), centrifugation time (Figure 3b), vortex agitation speed (Figure 3c), and the vortex time (Figure 3d). The default parameters were centrifugation at 1,200 g for 5 minutes, incubation for 5 minutes, and vortex agitation at 34.5 rps for 5 seconds unless otherwise varied. The normalized assay signals $S_{PED}(C)$ were plotted as a function of AS35 concentration *C* (Figure 3a-d), and also against both the operational parameters and AS35 concentrations in heat maps (Figure 3e-h). It was clear that the AS35 antibodies could be detected with a large contrast in signal S_{PED}, i.e. a high value at low concentrations ($S_H = S_{PED}(NC) \cong 1$, color-coded as red) and a small signal at high concentrations ($S_L = S_{PED}(C_H) \cong 0.1$, $C_H = 4\mu M$, color-coded as blue), or $\Delta S_{PED} = S_H - S_L \cong 0.9$. A high signal contrast indicated that the AuNP sensors effectively participated in the biochemical reaction at high protein concentrations and subsequently precipitated, which was ideal for maximizing the sensitivity and dynamic range (or about 9 logs in this test).

Clearly, the sensing performance of NasRED could be optimized within a range of centrifugation conditions, i.e., from 900 g to 1500 g and from 3 to 5 minutes, and at moderate vortex conditions. These observations can be understood from the unique features of NasRED. Fundamentally, NasRED is an in-solution assay, where diffusion and biochemical reactions between AuNP sensors and reagents drive the signal transduction and determine the assay performance. In NasRED, the sedimentation time of AuNPs can be expressed as $\tau_{sed} = z/(s \cdot g)$, where z is the precipitation length, g is the gravitation constant, and s is the sedimentation coefficient determined by AuNP diameter, buffer density, and buffer viscosity[24]. Unlike conventional assays, such as ELISA, which relies on the passive diffusion of target molecules to a stationary reaction surface and long incubation time to maximize the signal-to-noise ratio, NasRED supports external controls, such as centrifugation and vortex agitation, to actively

accelerate diffusion, reaction, and readout. Here, the centrifugation significantly reduces the precipitation length of clustered AuNPs from a few millimeters (here, the height of colloid liquid) to a micrometer scale (determined by precipitates at the tube bottom) and accordingly shortens the readout time to minutes. In comparison, passive precipitation of AuNP clusters was previously found to require 3 to 5 hours of assay time from mixing to readout[22]. In the meanwhile, centrifugation also localizes AuNPs and their clusters at a greatly boosted concentration at the bottom of the reaction tube, thus changing the dynamic equilibrium of antigen-antibody reaction to favor AuNP cluster formation even at ultralow reagent concentration in the tube[22]. On the other hand, vortex agitation is needed to resuspend monomer AuNPs not incorporated into clusters back to free-floating to ensure high specificity, i.e. the negative control should return to their initial states. However, excessively high agitation breaks the AuNP clusters biochemically "glued" together and would negatively affect the sensitivity.

Demonstration of antibody detection in PBS and biological fluids

To better determine the sensitivity of NasRED, we first performed NanoSight analysis (Figure S4-5) and found that the AuNP concentrations C_{AuNP} correlated linearly with the measured electronic signals S_{PED} (Figure S6). Noticeably, a significant amount of AuNPs were still free-floating when the tubes started to turn transparent (e.g. S_{PED}<0.1, or OD<~0.2), and such AuNPs were sufficient to produce noticeable optical extinction and, therefore, PED signals, because of a long optical path between the LED and photodetector (~5 mm). Then, SARS-CoV-2 antibody AS35 was spiked in PBS buffer, serum, and 20% diluted whole blood from 400 nM to 40 aM, and analyzed following our above-established sensing protocol (Figure 4a). The precipitate samples collected at the bottom of the tubes were imaged by Cryogenic electron microscopy (cryo-EM),

and AuNP clusters were found in the AS35 samples at low concentrations (4 fM and 40 aM, Figure 4b-c and Figure S6), while mainly AuNP monomers were found from the NC sample (Figure 4d). Statistical analyses (Figure 4e) confirmed that only small-sized (<2 μm) AuNP clusters were found for the NC samples, which could be attributed to nonspecific interactions between the AuNPs during centrifugation and/or sample preparation from pipetting, TEM grid loading, and freezing, but much larger AuNP clusters were found at 40 aM (mostly 1 to 20 μm but as large as 25 μm) and 4 fM (mostly 1 to 100 μm, as large as ~300 μm). The Cryo-EM imaging provided direct physical evidence to confirm the feasibility of detecting antibodies at attomolar levels using functionalized AuNP sensors.

Next, the NasRED sensitivity of antibody detection in HPS and 20% diluted human WB was studied (Figure 4f-j, Figure S7). Unlike PBS buffer, human sera contain proteins, amino acids, and antibodies and are more viscous[25,26]. WB further contains various blood cells and platelets, which may introduce additional hindrances to protein binding. In addition, hemoglobin in the WB strongly absorbs blue and green light to produce a red color[27], which could interfere with the solution color and electronic signals. To counter the physical and chemical impacts, WB was diluted to 20% to ensure sufficient light passage, and the sensing protocols (Table S2, Figure S8) were adjusted to increase the centrifugation speed to 1,500 g, the incubation time to 20 minutes, and the vortex force to 37.2 rps. This modified protocol facilitated the formation of AuNP precipitates (Figure 3e-f, and Figure S6) at the tube bottoms for the antibody samples in both HPS and WB, similar to those formed in PBS. Further, 5 μL of the WB supernatants were collected and loaded in a PDMS plate to quantify the optical extinction on a lab spectrometer (Horiba) (Figure 4i, complete data in Figure S8e). The normalized electronic and optical signals (Figure 4j) were used to determine the LoDs as 66 aM, 76 aM, and 701 aM, respectively, for antibody detection in

PBS buffer, serum, and 20% WB with PED readout, and ~100 aM in WB with spectrometer readout.

The consistently observed ultrahigh sensitivity of NasRED can be attributed to its unique signal transduction mechanism, which is initiated by biochemical protein reaction and subsequently modulated fluidic dynamically during AuNPs precipitation. TEM imaging revealed that multi-layered densely stacked AuNP clusters formed in the core of the precipitates (Figure S6), while some AuNP monomers, particularly those at the perimeters of AuNP clusters, were separated by a much larger distance (e.g., 40 to 100 nm) than the size of the protein complex (streptavidin, RBD, and AS35). It is, therefore, hypothesized that the chemically initiated AuNP clustering creates a 3D core in the precipitates, and these core clusters further physically recruit and localize additional AuNP monomers and oligomers at their perimeters by disrupting the fluidic flow during centrifugation and vortex agitation and/or trapping through electrostatic interactions. In this case of detection in WB, blood cells also precipitated to the tube bottom after centrifugation (a schematic shown in Figure S7c). They might also contribute to fluidic and electrostatic interactions with AuNP clusters and monomers that helped amplify the sensing signals and improve the sensitivity.

To find out the reproducibility of the proposed NasRED biosensor, three replicates of antibody samples in PBS as well as 20% WB were tested (Figure S9). Despite small deviations in readout signals, attomolar-level LoDs were found consistently for both the PBS and blood samples. Further data fitting analyses revealed that even lower LoDs were obtained using a biphasic dose response[28] rather than a simple sigmoidal model. While more theoretical and experimental investigations in the future are apparently needed to completely decipher the underlying mechanisms, it is hypothesized that the affinity-driven, biochemical protein binding and the centrifugation/vortex-

driven fluidic dynamic interactions work as two mechanisms that affect the AuNP clustering and the subsequent signal transduction in the NasRED assay, thus effectively creating two phase transitions in the response curves. Nevertheless, despite physical, chemical, and optical interferences, these experimental analyses consistently proved the feasibility of high-sensitivity antibody detection in complex biological fluids, demonstrating the capability and versatility of NasRED in disease diagnostics and immunology.

N-protein antigen detection in biological fluids

NasRED was also demonstrated for SARS-CoV-2 antigen detection by functionalizing the AuNPs, using commercially available monoclonal antibodies (AS47 and AM223, both from Acrobiosystems) targeting the N-protein in PBS (Figure 5a-c). Interestingly, sensing using AS47-functionalized AuNP sensors displayed a poor color contrast ($S_{PED}(NC) - S_{PED}(400nM) \cong 0.2$) (LoD 308 pM), and AM223-AuNP sensors produced more differentiable optical contrasts (LoD 4.7 pM), and finally the use of two sets of AuNPs, functionalized with AS47 and AM223, respectively, produced the best signal contrasts and dynamic range (LoD 470 aM). The co-binding AuNP sensors also produced LoDs of 870 aM for N-proteins spiked in saliva and 4.1 fM in nasal fluid (Figure 5d-f). This greatly enhanced sensitivity was attributed to the improved binding avidity because the two mAbs cooperatively target distant, non-overlapping epitopes of the N-protein (AS47 on the C terminus side and AM223 on the N-terminus side), which favors much more stable protein complex formation and accordingly larger AuNP clusters upon antibody-antigen binding[22]. On the other hand, the cobinder-based NasRED sensors could easily differentiate SARS-CoV-2 from HCoV-NL63 and HCoV-229E, which cause the common cold and result in similar symptoms to SARS-CoV-2 infection (Figure 5g-h). In fact, even 4 fM SARS-

CoV-2 N-protein produces a signal (S_{PED}~0.63, Figure 1f) differentiable from 400 nM HCoV-NL63 and HCoV-229E (S_{PED}~0.95, Figure 1f), indicating a very high specificity of the NasRED system.

We further demonstrated direct detection of inactivated SARS-CoV-2 virion particles using the antigen sensors (Figure 6) by mixing the AuNP sensor buffer with PBS-diluted viruses (by 10 log titrations) and lysis reagents (Triton X-100, 0.3% v/v concentration) to extract N-proteins (Methods). By referring to the initial concentrations of N-proteins (determined as 2995 ng/mL or ~30 nM by ELISA) and RNA copy numbers (4.7×10^9 copies/mL by quantitative PCR, Table S4), the LoDs were found 422 aM (21 fg/mL) for the N-protein and 33 copies/ml for the RNA. Given the fundamental limitations of ELISA and qPCR in quantitation and possible impure RNA and/or N-proteins in the sample (ZeptoMetrix), the results clearly indicated that NasRED achieved high sensitivity outperforming ELISA and qPCR.

Discussion

In the NasRED platform, AuNP sensors play a few roles in promoting the assay performance, because they can improve multivalent protein binding[29,30], create a concentration-boosting effect after centrifugation to further promote the protein-antibody interactions even at low concentrations, accelerate signal readout from AuNP clustering and their sedimentation, act as an effective optoelectronic beacon to scatter light and help produce electronic signals from a simple NasRED system rather than sophisticated microscopy and spectrophotometers, and minimize adverse nonspecific interactions with different proteins and biological media. These design considerations also make NasRED a unique breakthrough technology superior to ELISA[31]and many antigen tests[32–36], particularly considering the compromise between sensitivity and other

performance metrics, such as the assay time, cost, complexity of the readout instrumentation, sample volume, etc., does not apply to NasRED. For example, LFA have gained tremendous attention and broadened use during the COVID-19 pandemic because of their relatively low cost (~$10), rapid turnaround time (~15 min), and more straightforward sample preparation and detection schemes[37]. However, LFAs usually have poor sensitivity (e.g. about 25 ng/mL[21], Table S5). On the other hand, ELISA demonstrated high sensitivity (e.g. 8.4 pg/mL, Table S6), but its use is limited due to its higher test cost [31], bulky and costly instrument (e.g. ~$10,000 for Agilent BioTek 800 TS Absorbance Reader), long turnaround time (typically hours), and requirement of specially trained personnel. In comparison, NasRED achieved prominent sensitivity (39 fg/mL or 184 fg/mL in saliva and nasal fluid) that is >6,000 times better than LFA[21] and ~50 times better than ELISA[31], with only about 15 to 30 minutes from sample mixing to readout, including 5 minutes centrifugation, 5 minutes (for antibody sensing) or 20 minutes (for antigen sensing) incubation, a few seconds vortex agitation, and PED readout. In addition, NasRED performs tests in microcentrifuge tubes without any labeling, washing, or enzymatic reaction, therefore reducing the number of processing steps and minimizing sample volume (only 6 µL, much smaller than a single drop of blood) and reagent usage[22,23]. If using commercially available streptavidin-coated AuNPs (Cytodiagnostics), the AuNP sensing solution cost is ~$0.1 per µL, or ~$1.8 per test (18 µL). However, large-scale production of streptavidin-functioned AuNPs by solution synthesis from $HAuCl_4$ and streptavidin can further significantly lower the cost of AuNP sensors. Thus, the overall cost of materials and reagents could be ~$2 per test at small-scale prototyping and can be <$1 if produced at scale[22,23]. These results suggest that our sensing platform can be made accessible in low-resource settings where a high-sensitivity test is currently unavailable. We believe future development, such as integration and automation of centrifugation, vortex, and data

analysis processes, which is highly feasible electronically, can create a portable platform that can be deployed not only in clinics, hospitals, and community centers but also in the field next to the users.

Methods

Sources of reagents and instrumentation

Biotinylated WT-RBD (Wuhan-Hu-1), AS35 anti-SARS-CoV-2 antibody, biotinylated anti-SARS-CoV-2 Nucleocapsid antibody, Chimeric mAb, Human IgG (AM223), mouse IgG (AS47) and SARS-COV-2 Nucleocapsid protein were commercially purchased from ACROBiosystems. Triton^{TM} X-100 was purchased from Millipore Sigma. The microcentrifuge (accuSpin Micro 17) and the vortexer (Analog Vortex Mixer Catalog No. 02-215-365 for antibody detection and Digital Vortex Mixer Catalog No. 02-215-418 for antigen detection) were both purchased from Thermo Fisher.

Electronic readout system

The NasRED readout system (Figure S1) included a reading device and a circuit board for signal processing. The reading device consisted of three main components: an LED (WP7113PGD, Kingbright), a photodiode-integrated circuit (SEN-12787, SparkFun Electronics, integrated with a digital light-sensor APDS-9960 from Broadcom), and a microcentrifuge tube holder that was 3D printed (Qidi Tech X-Plus 3D Printer) using black carbon fiber polycarbonate filament to fit snugly into a standard 0.5 mL Labcon microcentrifuge tube. An alkaline battery (9V) was converted to 5V by a voltage regulator circuit as the power supply. The photodiode APDS-9960 was biased at 3.3 V and interfaced with a microcontroller (Atmega328) to convert the output into a digital signal. The regulator circuit was comprised of two electrolytic capacitors (10 µF), two ceramic capacitors (0.1 µF), and one protective Zener diode (Figure 2a (i)). The constant current LED driver circuit utilized a feedback loop to stabilize the current supplied to the LED. For example, a sudden increase in the base voltage of transistor T2 ($V_{B,2}$) would increase its base-to-emitter bias ($V_{BE,2}$) and, therefore, conduct a higher amount of current ($i_{LED}= i_{C,2}\approx i_{E,2}$) through the LED and the T2

collector, which would tend to cause the LED current to rise. However, the higher $i_{E,2}$ would also boost the voltage drop across resistor R3, or the base-to-emitter bias voltage of transistor T1 ($V_{BE,1}$). This, in turn, would lead to enhanced emitter current ($i_{E,1}$) and collector current ($i_{C,1} \approx i_{E,1}$). This increase in $i_{C,1}$ would cause larger voltage drop across resistor R2, and, therefore lower $V_{B,2}$ to counter the voltage fluctuation and stabilize the LED signals. All the above electronic components, including microcontroller, capacitors, resistors, transistors, etc., were purchased from DigiKey unless specified otherwise.

Polydimethylsiloxane (PDMS) well plate fabrication

Sylgard 184 silicone elastomer base was thoroughly mixed with the curing agent (mass ratio 10:1) for 30 minutes in a petri dish and placed in a vacuum container for 2 hours to degas. The mixture was then fully cured at room temperature into a PDMS membrane, which was then cut to the desired size and punched to create 2 mm wells. The as-prepared PDMS membrane and a diced fused silica chip (500 μm thick) were rinsed with isopropyl alcohol, dried by nitrogen, and treated with oxygen plasma. Immediately after, the two were bonded to form a PDMS well plate. The PDMS plate was treated with 1 wt% PVA in water solution for 10 minutes to prevent the non-specific binding of proteins, adapted from previously reported methods[38]. Finally, it was dried with nitrogen, heated on a 110°C hotplate for 15 minutes, and cooled to room temperature.

1×PBS dilution buffer

The 10× Phosphate-buffered saline (PBS, Fisher Scientific) stock buffer was mixed with glycerol (Sigma-Aldrich) and BSA (Sigma-Aldrich) and deionized water (Fisher Scientific) to create a 1×PBS dilution buffer with a final concentration of 1×PBS, 20 % v/v glycerol, and 1 wt % BSA. This dilution buffer (pH~7.4) was used to prepare the AuNP sensors, antigen and antibody solutions, and diluted biological media.

Sensing solution preparation and quantification

Streptavidin-functionalized AuNPs (~0.13 nM, 80 nm, OD10) were purchased from Cytodiagnostics, and quantified by Nanosight (NS3000, Malvern Panalytical). To create AuNP sensing solution (e.g. 200 μL, OD = 0.5), the streptavidin-coated AuNPs (50 μL, OD10) were mixed with an excessive amount of biotinylated antigens or antibodies (e.g. about 1.2 μM, 20 μL), incubated for 2 hours, diluted by adding 1000 μL of 1×PBS dilution buffer and purified by centrifugation at 9,600 g for 10 minutes, followed by removing 1050 μL supernatant and adding 1050 μL 1×PBS dilution buffer. The above purification was repeated another time to remove unbound biotinylated antigens or antibodies. The purified sensing solutions were measured by Nanodrop 2000 (Thermo Fisher) to determine the AuNP concentration and then adjusted to the desired optical extinction level (e.g., in our case ~0.048 nM for 80 nm AuNPs) by mixing with 1×PBS dilution buffer. Prior to each sensing experiment, the stock sensing solutions were aliquoted into Eppendorf tubes of 18 μL each.

Antibody and antigen detection in biological buffer

Sensing in PBS: The target antigen (N-protein) or antibody was adjusted to a target concentration (e.g., 40 aM to 4 μM) by mixing with 1×PBS dilution buffer. Then 6 μL of such antigen or antibody solutions were mixed with an 18 μL AuNP sensing solution, followed by vortex agitation at 34.5 rps for 5 seconds. The final antigen or antibody concentration in the mixed reaction buffer (24 μL) was therefore diluted four times from the original solutions, e.g. 40 aM to 10 aM and 4 μM to 1 μM.

Biological media preparation: Human Pooled Serum (HPS) was used as purchased. Human whole blood (WB) was diluted with 1×PBS dilution buffer to 20%. Saliva and nasal fluid were purified by centrifugation at 9,600 g for 5 minutes to precipitate the mucus, and the supernatant

was used. Their corresponding final concentration in the sensing mixture was 25% HPS, 25% nasal fluid, 25% saliva, and 5% WB. Single donor human WB, HPS, human nasal fluid, and saliva were purchased from Innovative Research, Inc.

Inactivated virus N-protein extraction: PROtrol SARS-CoV-2 (Isolate: USA-WA1/2020) was purchased from ZeptoMetrix LLC in standard Vero E6 culturing medium (2% minimum essential medium (MEM)). The N-Protein was extracted by adding 0.6% v/v Triton X-100 (non-ionic surfactant, from Millipore Sigma) at a 1:1 v/v ratio to the SARS-CoV-2 sample, followed by 5 minutes incubation to release the N-protein via viral envelope micellization[39,40].

qPCR assay was performed by ZeptoMetrix, and the protocol and the data were shared with their permission. The SARS-CoV-2 viral RNA was extracted from 200 µL of PROtrol sample (part # PROSARS(COV2)-587) using QIAmp MinElute Virus extraction. Briefly, the sample was lysed using the lysis buffer (NaCl, Tris-HCL, SDS), followed by RNA binding to silica in a spin column, sequentially washed by guanidine hydrochloride and ethanol to remove impurities and salts, and the viral RNA was eluted into 60 µL of aqueous viral elution (AVE) buffer (RNase-free water, 0.04% Sodium Azide (NaN3)) and immediately used to measure genomic copies in real-time quantitative PCR assay. Furthermore, the RNA from working quantitative standard and extraction control were extracted alongside the PROtrol samples. The extracted SARS-CoV-2 RNA was tested in the SAR-CoV-2 qRT-PCR assay that targets the N protein-coding gene. The PCR reaction buffer included 6.25 µL TaqMan Fast Virus 1-Step Multiplex Master Mix for qPCR (carboxy rhodamine dye free), 1 µL of each forward and reverse primers at 500 nM final concentration, 1 µL fluorescent probe at 200 nM final concentration (Table S3), 5 µL of extracted RNA as PCR template, and 11.75 µL RNase-free water (25 µl total mixture volume). PCR was run in a QuantStudio 5 System. A standard curve was generated using 10-fold serial dilutions of the

extracted RNA from a working standard with known copies/mL, determined by droplet digital PCR (ddPCR). The same 10-fold serial dilutions were made with the extracted RNA from the PROtrol sample (n=2 sets) and tested against the standard curve to determine the quantity of viral RNA in the PROtrol sample. The working standard and the PROtrol qPCR data was analyzed using the QuantStudio Design & Analysis Software (V1.4.3).

NasRED data processing

The NasRED data analysis involved signal collection, calibration, and normalization. First, the target proteins in biological media were measured on the designed PED device, together with a negative control (NC, 18 µL functionalized AuNPs mixed with 6 µL biological medium without target proteins). Then, each sample tube (18 µL AuNP sensing solution mixed with 6 µL target protein solution, in total 24 µL) and the NC tube underwent measurements along five orientations relative to a tube holder position to account for tube variations and inhomogeneous matrix optical impacts such as turbidity and color. The measured digital photodiode sensor signals for each sample tube were averaged, collected to a datasheet (.csv), and saved to a predefined local folder on a computer, all automated by Python scripts. The averaged sample signals $T_0 = \frac{\sum_i (T_{0,i}(C))}{5}$ (i=1 to 5 for the five measurements, at protein concentration C) represented the total optical transmission through the sample supernatant and the microcentrifuge tube right after mixing. After testing (through centrifugation, incubation, and vortex agitation), another five measurements were performed for each tube along the same orientations, and the electronic signals were again recorded as $T_t(C) = \frac{\sum_i (T_{t,i}(C))}{5}$ (i=1 to 5). Subsequently, the calibrated electronic signals, representing the difference in optical extinction caused only by the decrease of free-floating AuNPs due to precipitation, were calculated as $T_{D,i}(C) = T_{t,i}(C) - T_{0,i}(C)$, and $T_D(C) = \frac{\sum_i (T_{D,i}(C))}{5}$. The difference of NC signals before and after the test $T_D(NC) = T_t(NC) - T_0(NC)$ was also

calculated, and $T_D(NC)$ <5% $T_0(NC)$, i.e. most AuNPs redisperse and return to their original state right after mixing, was used as a criteria to validate the sensing protocol. Finally, considering the batch-to-batch difference in AuNP sensor concentrations as well as physical variations of biological fluids on the NasRED signals, the collected PED signals were further normalized to a range from 0 to 1 as $S_{PED}\ (C) = 1 - \frac{T_D(C)-T_D(NC)}{T(PC)-T_0(NC)}$. Here, a positive control signal (PC) was chosen for normalization purpose to represent the highest possible optical transmission, i.e. AuNPs completely precipitate. For mostly clear biological media, including PBS, saliva, nasal fluid, and serum, a mixture sample of 18 μL 1×PBS dilution buffer (representing sensing solution after AuNPs precipitate) and 6 μL biological media was used as a reference for simplicity, and the transmission signal was collected as the $T(PC)$. To account for the complex physical and chemical interactions between blood and AuNPs, the PC reference in WB was designed by mixing 18 μL WT RBD-coated AuNP sensing solution with 6 μL 20% WB spiked with high-concentration (C_H =800 nM) antibodies. In this case, the PC signals were defined as $T(PC) = T_t(C_H) - T_0(C_H) = T_D(C_H)$. In addition, the errors of the measurements were calculated as the standard deviation (SD) of the 5 normalized signals $SD(C) = \sqrt{\frac{\sum_i (T_{D,i}(C)-T_D(C))^2}{5(T(PC)-T_0(NC))^2}}$ (i=1 to 5, for the 5 measurement orientations). The normalized sensing signals $S_{PED}\ (C) \pm SD(C)$ were plotted against the antigen or antibody concentrations in each tested biological media. For the reproducibility experiment performed in this work, the average of each concentration measurement $\overline{S_{PED}}(C)$ was calculated as $\overline{S_{PED}}(C) = \frac{\sum_i (S_{PED,j}(C))}{3}$ (j=1 to 3 for the three replicate measurements) and the corresponding error was calculated as $\sqrt{\frac{\sum_j (SD_j(C))^2 + (SD(S_{PED,j}\ (C)))^2}{3}}$ (j=1 to 3 for the three replicate measurements). Here the within-test measurement errors $SD(C)$ and between-test

deviations $SD(S_{PED}(C))$ were considered to account for the variability of the repeated experiments[41].

Data fitting and LoD calculations

The normalized signals S_{PED} were fitted using Origin 2024b software (OriginLab, USA) by orthogonal distance regression algorithm to consider the data and error weight in fitting calculations. Dose-response model (or sigmoidal function) was used for fitting, following

$$S_{PED,DS}(C) = S_L + \frac{S_H - S_L}{1 + 10^{((\mathrm{Log}\ EC_{50} - \mathrm{Log}C) \times r)}}$$

where S_H and S_L were the highest and lowest sensing signals obtained from NC (or lowest concentrations) and the highest protein concentrations, respectively, EC_{50} was the half maximal effective concentration, and *r* describes the steepness of the sensing curve. In general, the EC_{50} and *r* values would determine the LoD. A large signal contrast $\Delta S_{PED} = S_H - S_L$, resulting from a small S_L (i.e. high level of AuNP precipitation), in combination with a small slope *r*, would be desired for obtaining a large dynamic range. In addition, a biphasic dose-response model was explored when a simple sigmoidal model failed to produce acceptable fitting, following

$$S_{PED,DS}(C) = S_L + \frac{S_{H1} - S_L}{1 + 10^{((\mathrm{Log}\ EC_{50,1} - \mathrm{Log}C) \times r1)}} + \frac{S_{H2} - S_L}{1 + 10^{((\mathrm{Log}\ EC_{50,2} - \mathrm{Log}C) \times r2)}}$$

where two sets of EC_{50}, S_H, and slope *r* values were used.

Fitting parameters were adjusted so that the goodness of fit parameters such as reduced Chi-square, R-squared coefficient of determination (COD), and reduced sum of squares (RSS) were calculated close to 1, 1, and 0, respectively. The LoD was then calculated such that the PED signal at this concentration on the fitted curve distinguished from the measured NC sample by 1.645 times the standard deviation of the NC and the lowest concentration sample[42,43] following $S_{PED,DS}(LoD) =$

$S_{PED}(NC) - 1.645 \times (SD(NC) + SD(C_{Min}))$, where C_{Min} was the lowest protein (antibody, antigen or virion particle) concentration.

Data fitting and LoD calculations

The normalized signals S_{PED} were fitted using Origin 2024b software (OriginLab, USA) by orthogonal distance regression algorithm to consider the data and error weight in fitting calculations. Dose-response model (or sigmoidal function) was used for fitting, following

$$S_{PED,DS}(C) = S_L + \frac{S_H - S_L}{1 + 10^{((\mathrm{Log}\, EC_{50} - \mathrm{Log} C) \times r)}}$$

where S_H and S_L were the highest and lowest sensing signals obtained from NC (or lowest concentrations) and the highest protein concentrations, respectively, EC_{50} was the half maximal effective concentration, and *r* describes the steepness of the sensing curve. In general, the EC_{50} and *r* values would determine the LoD. A large signal contrast $S_H - S_L$, resulting from a small S_L (i.e. high level of AuNP precipitation), in combination with a small slope *r*, would be desired for obtaining a large dynamic range. In addition, a biphasic dose-response model was explored when a simple sigmoidal model failed to produce acceptable fitting, following

$$S_{PED,DS}(C) = S_L + \frac{S_{H1} - S_L}{1 + 10^{((\mathrm{Log}\, EC_{50,1} - \mathrm{Log} C) \times r1)}} + \frac{S_{H2} - S_L}{1 + 10^{((\mathrm{Log}\, EC_{50,2} - \mathrm{Log} C) \times r2)}}$$

where two sets of EC_{50}, S_H, and slope *r* values were used.

Fitting parameters were adjusted so that the goodness of fit parameters such as reduced Chi-square, R-squared coefficient of determination (COD), and reduced sum of squares (RSS) were calculated close to 1, 1, and 0, respectively. The LoD was then calculated such that the PED signal at this concentration on the fitted curve distinguished from the measured NC sample by 1.645 times the standard deviation of the NC and the lowest concentration sample[42,43] following $S_{PED,DS}(LoD) =$

$S_{PED}(NC) - 1.645 \times (SD(NC) + SD(C_{Min}))$, where C_{Min} was the lowest protein (antibody, antigen or virion particle) concentration.

Spectrometry measurement in blood sample

AS35 was detected in 20% diluted human WB, following the modified protocol, and analyzed by spectroscopic measurements. Here, the samples' supernatant liquids (5 μL) were loaded into a PDMS well plate and measured by the spectrometer (iHR-320, Horiba Instruments Inc.). To achieve the best contrast, the focal plane was adjusted at the well plate surface, and then three spots were selected from within each well (one at the center and two near the edges) to account for possible inhomogeneity of AuNPs' distribution. The transmitted light was collected by a 50×objective lens (NA=0.8) from each spot, and the transmission spectra were measured 64 times from 350 to 750 nm range with 0.01 seconds integration time. The signals collected from the three spots were then averaged and normalized against the reflectance from a silver-coated mirror as $T_{PDMS}(\lambda, C)$, where λ was the wavelength, and C was the protein concentration. The optical extinction spectra were obtained as $E_{PDMS}(\lambda, C) = 1 - T_{PDMS}(\lambda, C)$, from which the values at λ=570 nm were selected as the signal $E_{test}\ (C)$. In addition, $E_{test}(PC) = E_{test}(C_H)$ was similarly collected for the positive control (18 μL WT RBD-coated AuNP sensing solution mixed with high-concentration (C_H=800 nM) antibodies spiked in 6 μL 20% WB), and $E_{test}(NC)$ was determined for the NC sample (sensing solution mixed with the biological medium at 3:1 ratio). The spectrometer signals were calculated as $S_{spec}\ (C) = \frac{E_{test}(PC) - E_{test}(C)}{E_{test}(PC) - E_{test}(NC)}$ and the error of the measurement was calculated as the standard deviation (SD) of the 3 normalized signals $SD_{spec}(C) = \sqrt{\frac{\sum_i (S_{spec,i}(C) - S_{spec}(C))^2}{3}}$ (i=1 to 3, for the 3 measurement spots).

Acknowledgements

We acknowledge support from Dr. D. Williams at Arizona State University for cryoTEM inspections, Dr. T. Zhang at Arizona State University for ELISA test, and Dr. Qin Xu at National Institutes of Health for helpful discussions. This project was supported in part by the National Science Foundation (NSF) under grant no. 1847324, U.S. Department of Agriculture AFRI 2022-67021-37013, and by the National Institute of Health under grant no. R21AI169098 and DP2GM149552. Access to the cryoTEM was supported, in part, by NSF grant no. ECCS-1542160.

Reference

(1) World Health Organization. *WHO COVID-19 dashboard*. https://covid19.who.int/ (accessed 2024-01-06).

(2) Walmsley, T.; Rose, A.; John, R.; Wei, D.; Hlávka, J. P.; Machado, J.; Byrd, K. Macroeconomic Consequences of the COVID-19 Pandemic. *Econ Model* **2023**, *120*, 106147. https://doi.org/10.1016/j.econmod.2022.106147.

(3) Myers, L. C.; Liu, V. X. The COVID-19 Pandemic Strikes Again and Again and Again. *JAMA Netw Open* **2022**, *5* (3), e221760. https://doi.org/10.1001/jamanetworkopen.2022.1760.

(4) Filip, R.; Puscaselu, R. G.; Anchidin-Norocel, L.; Dimian, M.; Savage, W. K. Global Challenges to Public Health Care Systems during the COVID-19 Pandemic: A Review of Pandemic Measures and Problems. *J Pers Med* **2022**, *12* (8), 1295. https://doi.org/10.3390/jpm12081295.

(5) World Health Organization. *Prioritizing diseases for research and development in emergency contexts*. https://www.who.int/activities/prioritizing-diseases-for-research-and-development-in-emergency-contexts (accessed 2024-01-06).

(6) UK Health Security Agency. *Emerging infections: how and why they arise*. https://www.gov.uk/government/publications/emerging-infections-characteristics-epidemiology-and-global-distribution/emerging-infections-how-and-why-they-arise (accessed 2024-01-06).

(7) Kubina, R.; Dziedzic, A. Molecular and Serological Tests for COVID-19. A Comparative Review of SARS-CoV-2 Coronavirus Laboratory and Point-of-Care Diagnostics. *Diagnostics (Basel)* **2020**, *10* (6), 434. https://doi.org/10.3390/diagnostics10060434.

(8) Reta, D. H.; Tessema, T. S.; Ashenef, A. S.; Desta, A. F.; Labisso, W. L.; Gizaw, S. T.; Abay, S. M.; Melka, D. S.; Reta, F. A. Molecular and Immunological Diagnostic Techniques of Medical Viruses. *Int J Microbiol* **2020**, *2020* (1), 8832728. https://doi.org/10.1155/2020/8832728.

(9) Katsanis, S. H.; Katsanis, N. Molecular Genetic Testing and the Future of Clinical Genomics. *Nat Rev Genet* **2013**, *14* (6), 415–426. https://doi.org/10.1038/nrg3493.

(10) Binny, R. N.; Priest, P.; French, N. P.; Parry, M.; Lustig, A.; Hendy, S. C.; Maclaren, O. J.; Ridings, K. M.; Steyn, N.; Vattiato, G.; Plank, M. J. Sensitivity of Reverse Transcription Polymerase Chain Reaction Tests for Severe Acute Respiratory Syndrome Coronavirus 2 through Time. *Journal of Infectious Diseases* **2023**, *227* (1), 9–17. https://doi.org/10.1093/infdis/jiac317.

(11) Eyzaguirre, E. J.; Walker, D. H.; Zaki, S. R. Immunohistology of Infectious Diseases. In *Diagnostic Immunohistochemistry*; Dabbs, D. J., Ed.; 2006; pp 43–64.

(12) Girt, G. C.; Lakshminarayanan, A.; Huo, J.; Dormon, J.; Norman, C.; Afrough, B.; Harding, A.; James, W.; Owens, R. J.; Naismith, J. H. The Use of Nanobodies in a Sensitive ELISA Test for SARS-CoV-2 Spike 1 Protein. *R Soc Open Sci* **2021**, *8* (9), 211016. https://doi.org/10.1098/rsos.211016.

(13) Vernet, R.; Charrier, E.; Grogg, J.; Mach, N. A Quantitative ELISA Protocol for Detection of Specific Human IgG against the SARS-CoV-2 Spike Protein. *Vaccines (Basel)* **2021**, *9* (7), 770. https://doi.org/10.3390/vaccines9070770.

(14) MacMullan, M. A.; Ibrayeva, A.; Trettner, K.; Deming, L.; Das, S.; Tran, F.; Moreno, J. R.; Casian, J. G.; Chellamuthu, P.; Kraft, J.; Kozak, K.; Turner, F. E.; Slepnev, V. I.; Le Page, L. M. ELISA Detection of SARS-CoV-2 Antibodies in Saliva. *Sci Rep* **2020**, *10* (1), 20818. https://doi.org/10.1038/s41598-020-77555-4.

(15) Shah, K.; Maghsoudlou, P. Enzyme-Linked Immunosorbent Assay (ELISA): The Basics. *Br J Hosp Med* **2016**, *77* (7), 98–101. https://doi.org/10.12968/hmed.2016.77.7.C98.

(16) Aydin, S. A Short History, Principles, and Types of ELISA, and Our Laboratory Experience with Peptide/Protein Analyses Using ELISA. *Peptides (N.Y.)* **2015**, *72*, 4–15. https://doi.org/10.1016/j.peptides.2015.04.012.

(17) Jegerlehner, S.; Suter-Riniker, F.; Jent, P.; Bittel, P.; Nagler, M. Diagnostic Accuracy of a SARS-CoV-2 Rapid Antigen Test in Real-Life Clinical Settings. *International Journal of Infectious Diseases* **2021**, *109*, 118–122. https://doi.org/10.1016/j.ijid.2021.07.010.

(18) Ndwandwe, D.; Mathebula, L.; Kamadjeu, R.; Wiysonge, C. S. Cochrane Corner: Rapid Point-of-Care Antigen and Molecular-Based Tests for the Diagnosis of COVID-19 Infection. *Pan Afr Med J* **2020**, *37*, 10. https://doi.org/10.11604/pamj.supp.2020.37.10.25982.

(19) Lin, Q.; Wen, D.; Wu, J.; Liu, L.; Wu, W.; Fang, X.; Kong, J. Microfluidic Immunoassays for Sensitive and Simultaneous Detection of IgG/IgM/Antigen of SARS-CoV-2 within 15 Min. *Anal Chem* **2020**, *92* (14), 9454–9458. https://doi.org/10.1021/acs.analchem.0c01635.

(20) Brandmeier, J. C.; Jurga, N.; Grzyb, T.; Hlaváček, A.; Obořilová, R.; Skládal, P.; Farka, Z.; Gorris, H. H. Digital and Analog Detection of SARS-CoV-2 Nucleocapsid Protein via an Upconversion-Linked Immunosorbent Assay. *Anal Chem* **2023**, *95* (10), 4753–4759. https://doi.org/10.1021/acs.analchem.2c05670.

(21) Pei, F.; Feng, S.; Hu, W.; Liu, B.; Mu, X.; Hao, Q.; Cao, Y.; Lei, W.; Tong, Z. Sandwich Mode Lateral Flow Assay for Point-of-Care Detecting SARS-CoV-2. *Talanta* **2023**, *253*, 124051. https://doi.org/10.1016/j.talanta.2022.124051.

(22) Chen, X.; Kang, S.; Ikbal, M. A.; Zhao, Z.; Pan, Y.; Zuo, J.; Gu, L.; Wang, C. Synthetic Nanobody-Functionalized Nanoparticles for Accelerated Development of Rapid, Accessible Detection of Viral Antigens. *Biosens Bioelectron* **2022**, *202*, 113971. https://doi.org/10.1016/j.bios.2022.113971.

(23) Ikbal, M. D. A.; Kang, S.; Chen, X.; Gu, L.; Wang, C. Picomolar-Level Sensing of Cannabidiol by Metal Nanoparticles Functionalized with Chemically Induced Dimerization Binders. *ACS Sens* **2023**, *8* (12), 4696–4706. https://doi.org/10.1021/acssensors.3c01758.

(24) Midelet, J.; El-Sagheer, A. H.; Brown, T.; Kanaras, A. G.; Werts, M. H. V. The Sedimentation of Colloidal Nanoparticles in Solution and Its Study Using Quantitative Digital Photography. *Particle and Particle Systems Characterization* **2017**, *34* (10), 1700095. https://doi.org/10.1002/ppsc.201700095.

(25) Leeman, M.; Choi, J.; Hansson, S.; Storm, M. U.; Nilsson, L. Proteins and Antibodies in Serum, Plasma, and Whole Blood—Size Characterization Using Asymmetrical Flow Field-Flow

Fractionation (AF4). *Anal Bioanal Chem* **2018**, *410* (20), 4867–4873. https://doi.org/10.1007/s00216-018-1127-2.

(26) Rosencranz, R.; Bogen, S. A. Clinical Laboratory Measurement of Serum, Plasma, and Blood Viscosity. *Am J Clin Pathol* **2006**, *125*, 78–96. https://doi.org/10.1309/fff7u8rrpk26vapy.

(27) Shenk, J. H.; Hall, J. L.; King, H. H. Spectrophotometric Characteristics of Hemoglobins. *Journal of Biological Chemistry* **1934**, *105* (4), 753–760. https://doi.org/10.1016/s0021-9258(18)75508-7.

(28) Calabrese, E. J. Biphasic Dose Responses in Biology, Toxicology and Medicine: Accounting for Their Generalizability and Quantitative Features. *Environmental Pollution* **2013**, *182*, 452–460. https://doi.org/10.1016/j.envpol.2013.07.046.

(29) Greenspan, N. S.; Cooper, L. J. N. Cooperative Binding by Mouse IgG3 Antibodies: Implications for Functional Affinity, Effector Function, and Isotype Restriction. *Springer Semin Immunopathol* **1993**, *15* (2–3), 275–291. https://doi.org/10.1007/BF00201107.

(30) Hornick, C. L.; Karush, F. Antibody Affinity-III the Role of Multivalence. *Immunochemistry* **1972**, *9* (3), 325–340. https://doi.org/10.1016/0019-2791(72)90096-1.

(31) Humbert, M. V.; Opurum, P. C.; Brendish, N. J.; Poole, S.; He, P.; Katis, I.; Quaye, J.; Bediako, Y.; Duriez, P. J.; Eason, R. W.; Sones, C.; Quaye, O.; Awandare, G. A.; Christodoulides, M.; Clark, T. W.; Quashie, P. K.; McCormick, C. J. A SARS-CoV-2 Nucleocapsid ELISA Represents a Low-Cost Alternative to Lateral Flow Testing for Community Screening in LMI Countries. *Journal of Infection* **2022**, *84* (1), 48–55. https://doi.org/10.1016/j.jinf.2021.08.049.

(32) iHealth. *iHealth COVID-19 antigen rapid test*. https://ihealthlabs.com/products/ihealth-covid-19-antigen-rapid-test?srsltid=AfmBOopp4Xjzv-uEyn7R7XCppH7XUWWWm0S3PSYqq57E2ldIP8bumQRS (accessed 2024-08-16).

(33) Genabio. *Genabio COVID-19 rapid self-test kit*. https://www.genabio.com/covid/ (accessed 2024-08-16).

(34) Abbott. *Abbott m2000 real-time*. https://www.molecular.abbott/us/en/products/infectious-disease/RealTime-SARS-CoV-2-Assay (accessed 2024-08-16).

(35) Viviani, T. *DiaSorin Simplex COVID-19 direct*. https://us.diasorin.com/en/molecular-diagnostics/kits-reagents/simplexa-covid-19-flu-ab-direct (accessed 2024-08-16).

(36) Matsumura, Y.; Shimizu, T.; Noguchi, T.; Nakano, S.; Yamamoto, M.; Nagao, M. Comparison of 12 Molecular Detection Assays for Severe Acute Respiratory Syndrome Coronavirus 2 (SARS-CoV-2). *Journal of Molecular Diagnostics* **2021**, *23* (2), 164–170. https://doi.org/10.1016/j.jmoldx.2020.11.007.

(37) Peeling, R. W.; Heymann, D. L.; Teo, Y. Y.; Garcia, P. J. Diagnostics for COVID-19: Moving from Pandemic Response to Control. *The Lancet* **2022**, *399* (10326), 757–768. https://doi.org/10.1016/S0140-6736(21)02346-1.

(38) Trantidou, T.; Elani, Y.; Parsons, E.; Ces, O. Hydrophilic Surface Modification of PDMS for Droplet Microfluidics Using a Simple, Quick, and Robust Method via PVA Deposition. *Microsyst Nanoeng* **2017**, *3*, 16091. https://doi.org/10.1038/micronano.2016.91.

(39) Dalgarno, P. A.; Juan-Colás, J.; Hedley, G. J.; Piñeiro, L.; Novo, M.; Perez-Gonzalez, C.; Samuel, I. D. W.; Leake, M. C.; Johnson, S.; Al-Soufi, W.; Penedo, J. C.; Quinn, S. D. Unveiling the Multi-Step Solubilization Mechanism of Sub-Micron Size Vesicles by Detergents. *Sci Rep* **2019**, *9* (1), 12897. https://doi.org/10.1038/s41598-019-49210-0.

(40) Roberts, P. L. Virus Inactivation by Solvent/Detergent Treatment Using Triton X-100 in a High Purity Factor VIII. *Biologicals* **2008**, *36* (5), 330–335. https://doi.org/10.1016/j.biologicals.2008.06.002.

(41) Monach, P. A. Repeating Tests: Different Roles in Research Studies and Clinical Medicine. *Biomarkers in Medicine*. 2012. https://doi.org/10.2217/bmm.12.57.

(42) Clinical and Laboratory Standards Institute. Protocols for Determination of Limits of Detection and Limits of Quantitation; Approved Guideline. NCCLS Document EP17-A. In *CLSI Document EP17-A*; 2004; Vol. 24.

(43) Armbruster, D. A.; Pry, T. Limit of Blank, Limit of Detection and Limit of Quantitation. *Clin Biochem Rev* **2008**, *29* (1), 49–52.

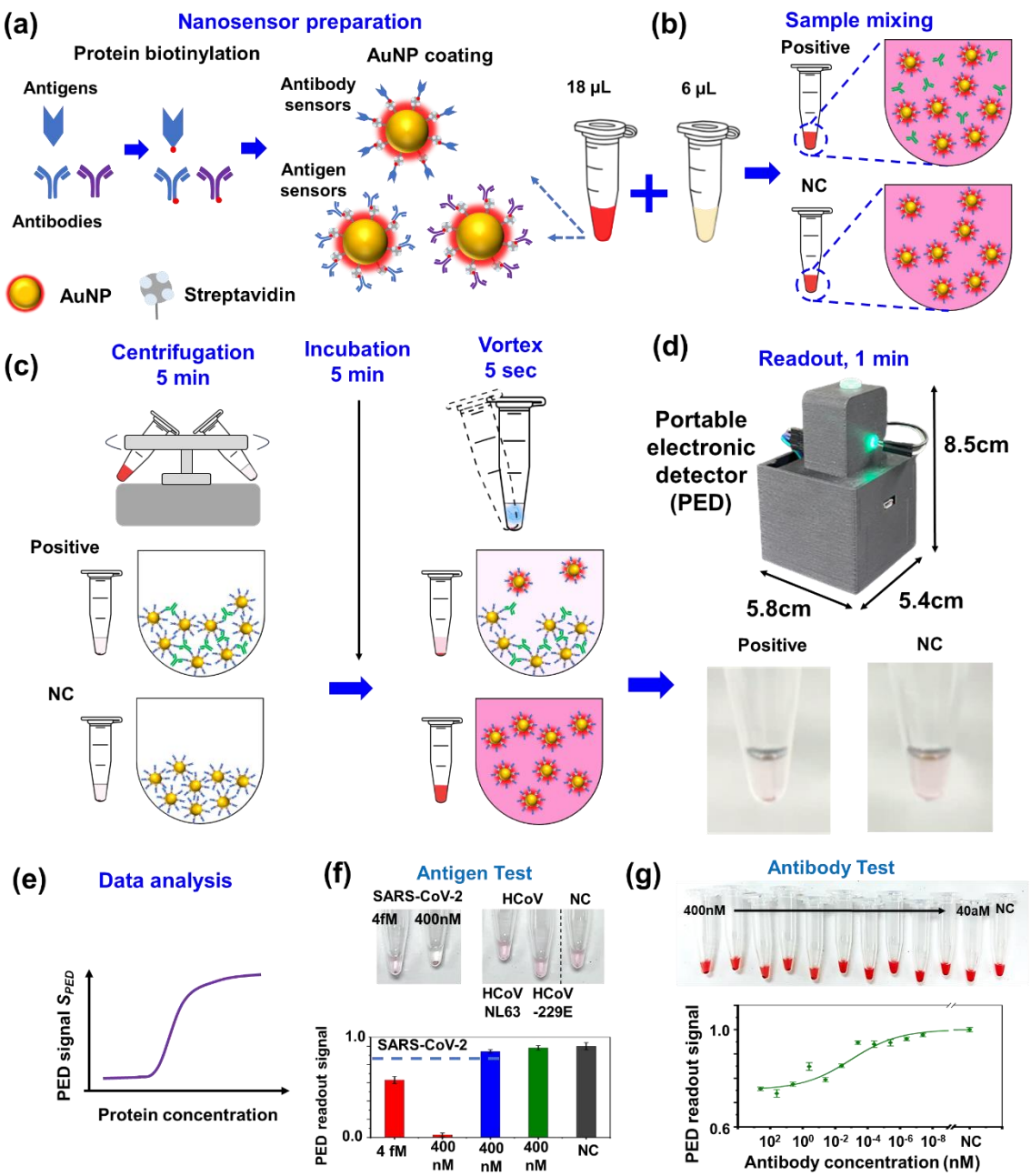

Figure 1: Nanoparticle-supported, rapid electronic detection of antigens and antibodies for infectious diseases. (a) Nanosensor preparation by biotinylating antigens or antibodies and attaching such proteins to streptavidin-coated AuNPs. (b-d) Schematics and optical images show the detection process, using antibody testing as an example. (b) The AuNP sensing solution (18 μL) was mixed with the medium solution (6 μL). Negative controls (NCs) did not contain any target molecules but otherwise contained the same biological fluids and AuNP sensors. (c) AuNPs were precipitated by centrifugation, incubated, and resuspended after vortex stirring. (d) The

readout was collected directly from the tube inserted in a tube holder as part of the NasRED readout system. The amount of AuNP precipitation at the bottom of the tube correlated with the number of test molecules, while no AuNP precipitates formed in the NC sample. (e) Schematic of a typical sensing curve of normalized PED readout signal S_{PED}. (f) Exemplary optical images and bar plots showing sensitivity and specificity in SARS-CoV-2 antigen detection in PBS. The tubes containing N-proteins of two other coronaviruses (HCoV-NL63 and HCoV-229E at 400 nM in PBS buffer) displayed very similar colors and electronic signals comparable to that of the NC sample. In contrast, the tubes with SARS-CoV-2 N-proteins showed much higher transparency and differentiable electronic signals at 4 fM and 400 nM. (g) Exemplary optical images and sensing curve plots showing antibody detection at high sensitivity in diluted whole blood.

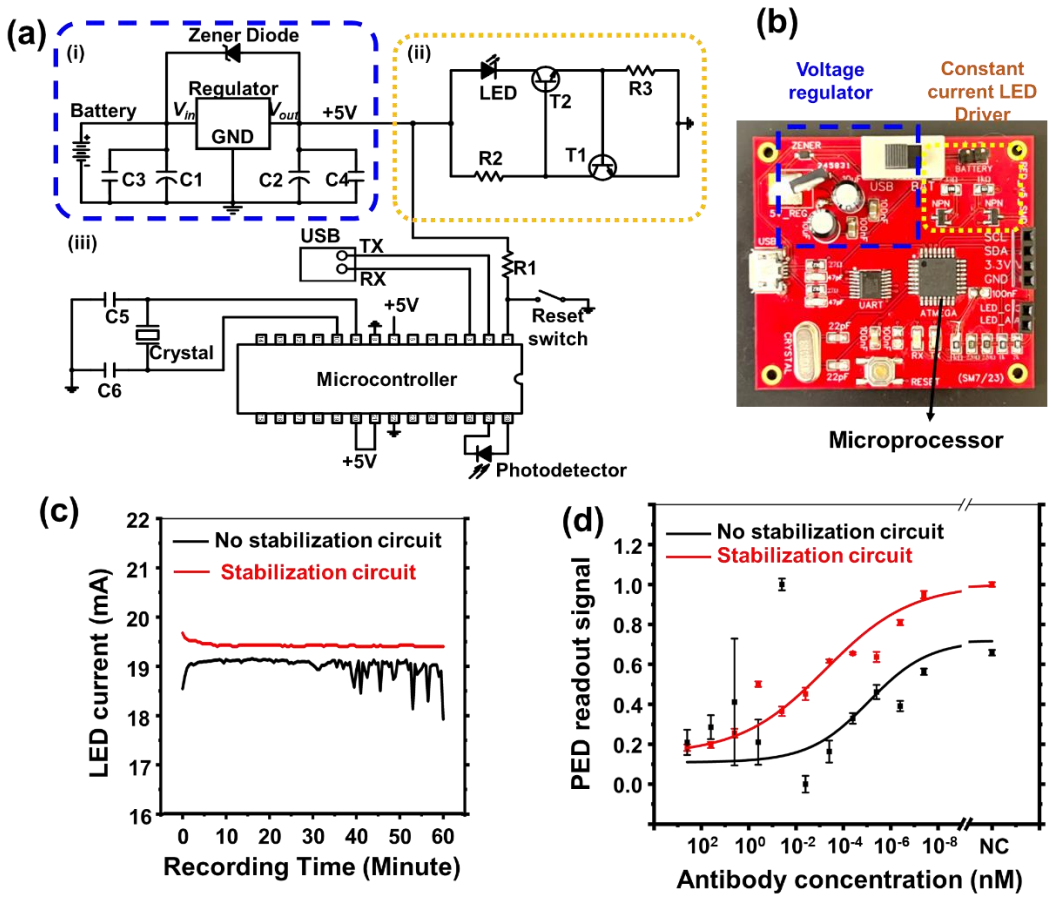

Figure 2: Electronic circuit design for stabilized NasRED readout. (a) Schematic showing an integrated printed circuit board (PCB) containing: (i) a built-in voltage regulator, (ii) a constant current LED driver circuit, and (iii) a microcontroller, which processes the signals and communicates with computers through USB, Wi-Fi, or Bluetooth modules. (b) Optical image showing the PCB board for signal processing. (c) The stability of LED currents over time for a circuit without the stabilization circuit (black line) and our integrated PCB board with the stabilization circuit (red line). (d) PED readout signal S_{PED} plotted against antibody AS35 concentrations spiked in PBS, with (red) and without (black) the stabilization circuit.

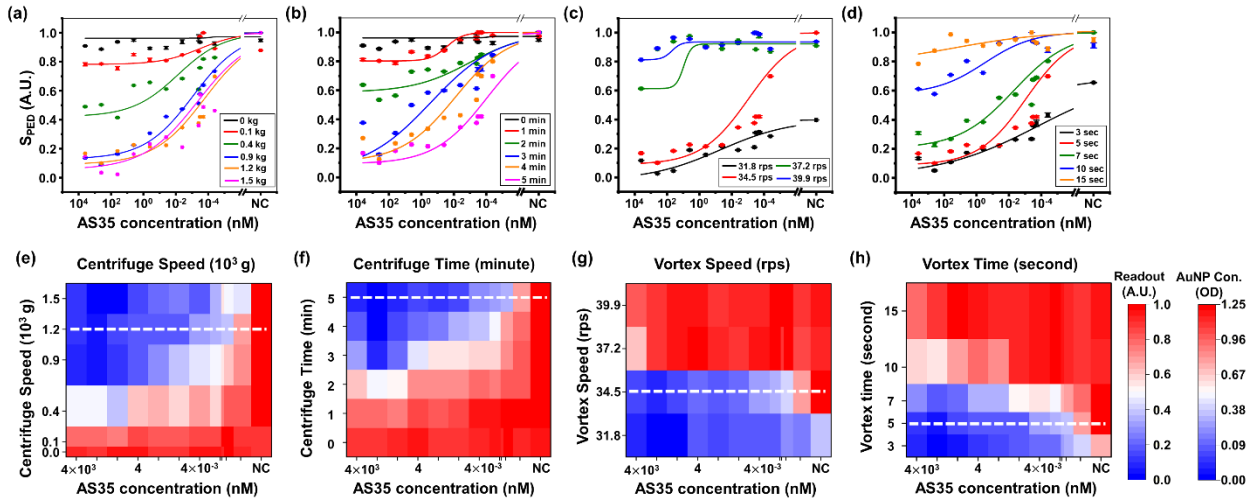

Figure 3: Optimization of NasRED sensing protocol at different centrifugation and vortex conditions. (a-d) The PED readout signal S_{PED} plotted as a function of the antibody concentration, with: (a) the centrifugate force from 0 to 1,500 gravity (g), (b) the centrifugation time from 0 to 5 minutes, (c) the vortex agitation speed from 32 to 40 round per second (rps), and (d) the vortex time from 3 to 15 seconds. (e-h) Heat maps showing the impacts of the above parameters and antibody concentrations on the detection signals. The default operation parameters were centrifugation at 1,200 g for 5 minutes (followed by 5 minutes incubation) and vortex agitation at 34.5 rounds per second (rps) for 5 seconds unless it was chosen as the variable. A high S_{PED} value contrast, i.e., close to 1 (color-coded as red) at low antibody concentrations and close to 0.1 (color-coded as blue) at high concentrations, was thought to be beneficial for simultaneously achieving a broad dynamic range and high sensitivity.

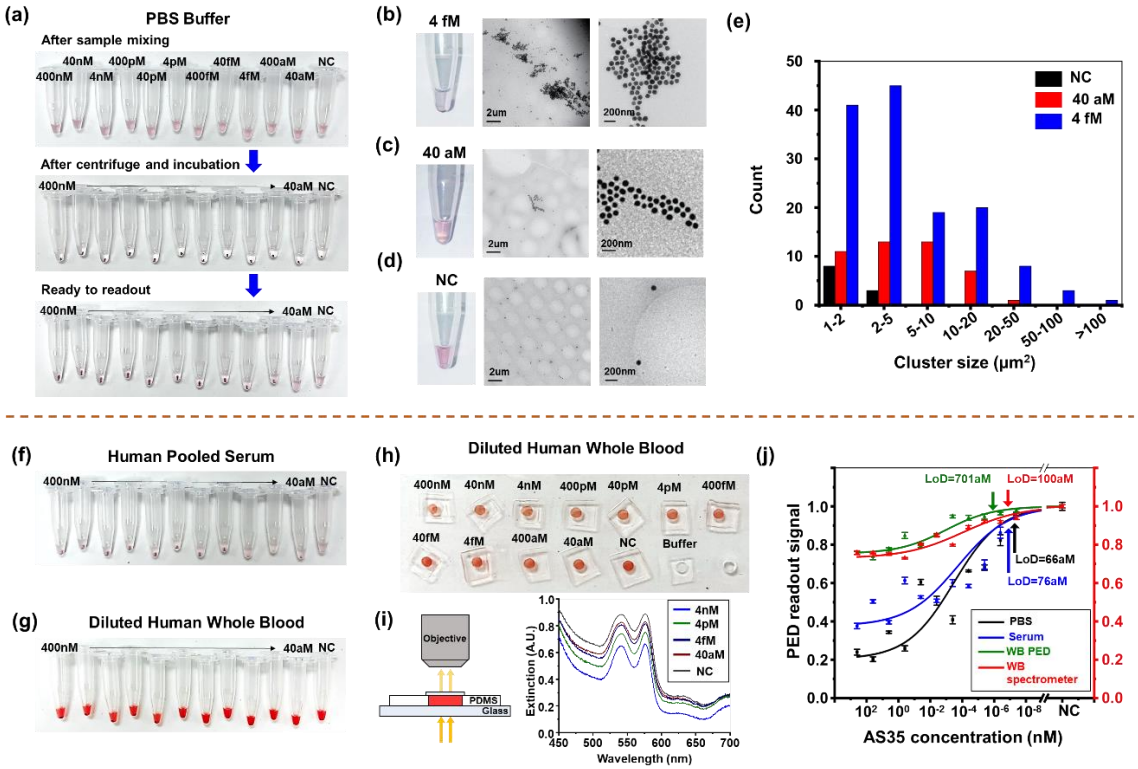

Figure 4: Microscopy and spectrometry confirmation of mAb AS35 detection in PBS and biological fluids. (a) Optical images show samples in PBS buffer at each key analysis step (centrifugation, incubation, and vortex agitation). The testing concentration ranged from 400 nM to 40 aM. NC: PBS only. (b-d) Representative cryo-TEM images of 80 nm AuNP clusters at AS35 concentrations of: (b) 40 fM, (c) 40 aM, and (d) NC. (e) Statistical analysis of AuNP cluster sizes formed at different AS35 concentrations. (f-g) Optical images showing samples ready for NasRED readout: (f) in human pooled serum and (g) in 20% diluted human whole blood. Upon mixing with the AuNP sensing solution, the HPS sample was 25% diluted, and the WB was 5% diluted. (h) The supernatant blood samples were loaded in a PDMS plate for spectrometer measurement of the optical transmission. (i) Schematics of spectroscopy characterization of antibody-spiked blood samples and the extracted optical extinction spectrums plotted as a function of wavelength for antibody concentrations (40 aM- 4 nM). (j) Extracted PED signals plotted against antibody concentration in PBS buffer (black line, LoD=66 aM), serum (blue line, LoD=76 aM), and whole blood (green line, LoD=701 aM). The optical extinction signals from the spectrometer were plotted against antibody concentration in whole blood (red line), showing a LoD of ~400 aM. The samples were analyzed using a standard testing condition, i.e., centrifugation at 1,200 g for 5 minutes, incubation for 5 minutes, and vortex agitation at 34.5 rps for 5 seconds.

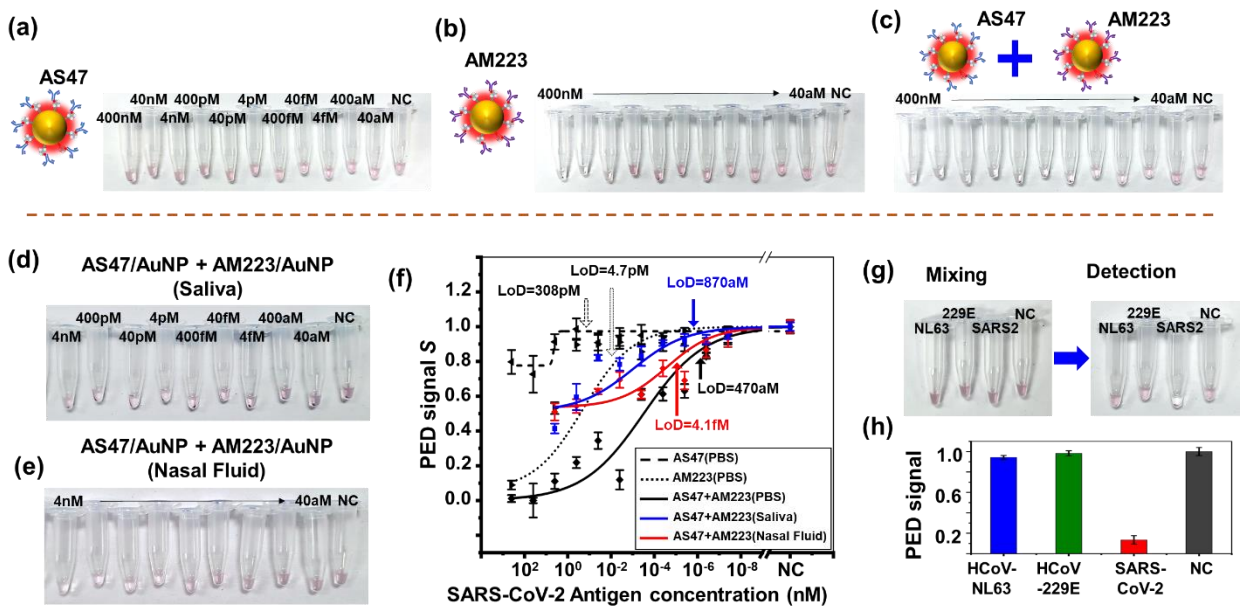

Figure 5: SARS-CoV-2 N-protein antigen detection in biological fluids**.** (a-c) Optical images showing antigen samples using AuNPs functionalized with different mAbs in PBS buffer: (a) only AS47, (b) only AM223, (c) co-binder (AS47 and AM223) on two sets of AuNPs. The final antigen concentrations ranged from 400 nM to 40 aM. NC: buffer only. (d-e) Optical images showing antigen samples ready for NasRED readout: (d) in human saliva, and (e) in human nasal fluid. The samples were centrifuged at 1,500 g for 5 minutes, incubated for 20 minutes, and vortex-stirred at 26 rps for 5 seconds. (f) Extracted PED signals plotted against antigen concentration in PBS buffer with different AuNP sensors, i.e. AS47/AuNP (black dashed line, LoD=308 pM), AM223/AuNP (black dotted line, LoD=4.7 pM), and cobinders (AS47/AuNP + AM223/AuNP, black solid line, LoD=470 aM), as well as antibody testing with the cobinders in saliva (blue solid line, LoD=870 aM) and nasal fluid (red solid line, LoD=4.1 fM). (g) Optical images showing samples for specificity test in PBS against human coronavirus (HCoV) (HCoV-NL63 and 229E) and SARS-CoV-2 N-proteins. All N-proteins were at 400 nM. (h) Extracted PED signals plotted against HCoV and SARS-CoV-2 antigens, as shown in figure g.

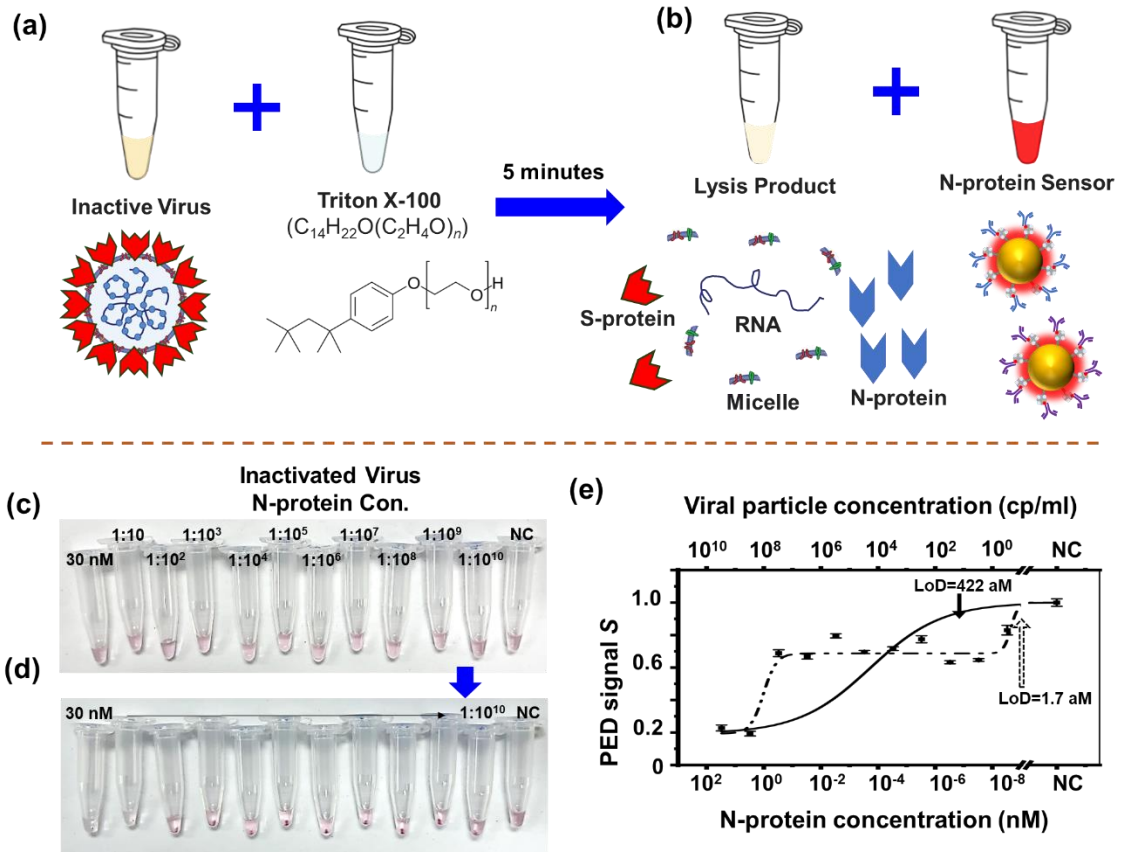

Figure 6: SARS-CoV-2 antigen detection from inactivated virion particles. (a-b) Schematics of preparing the inactive virus sample: (a) lysis using triton x-100 to produce product comprising viral RNA and proteins, and (b) mixing the lysis product with NasRED antigen sensor solution for viral N-protein detection. (c-d) Optical images showing a titration of the inactive virus samples: (c) after mixing with cobinder sensors (AS47/AuNP + AM223/AuNP) and (d) ready for NasRED readout. (e) PED signals plotted against inactivated virus N-protein concentration determined by ELISA (bottom x-axis) and the viral particle RNA count determined by qPCR (top x-axis) in PBS buffer. The PED signal was fitted using sigmoidal model (solid line, LoD=32 copies/ml or 422 aM) and biphasic dose-response model (LoD=0.13 copies/ml or 1.7 aM).

Table 1: NasRED design and performance in detecting SARS-CoV-2 antigens and antibodies

Target Molecules	**Medium**	**Protein binder**	**Centrifuge speed/time**	**Incubation time**	**Diagnostic sensitivity (Sigmoidal model)**	
					aM	**pg/mL**
Antibody AS35	PBS	WT-RBD	1,200 g, 5min	5min	66	0.01
	HPS	WT-RBD	1,200 g, 5min	5min	76	0.011
	20% WB	WT-RBD	1,200 g, 5min	20min	47×10^3	7
		WT-RBD	1,500 g, 5min	20min	701	0.105
SARS-CoV-2 N-protein	PBS	AS47	1,200 g, 5min	20min	308×10^6	14×10^3
		AM223	1,200 g, 5min	20min	4.7×10^6	212
		AS47/AM223	1,200 g, 5min	20min	470	0.021
	Saliva	AS47/AM223	1,200 g, 5min	20min	870	0.039
	Nasal fluid	AS47/AM223	1,200 g, 5min	20min	4.1×10^3	0.184
SARS-CoV-2 virion particles	PBS	AS47/AM223	1,200 g, 5min	20min	422	0.021
					32 RNA copies/mL	

Note, the vortex agitation was 5 seconds for all tests, but an Analog Mixer (at 2,100 rpm) was used for antibody and virion particle detection and a Digital Mixer (at 1550 rpm) was used for antigen detection.

Supplementary information for

Nanoparticle-Supported, Rapid, and Electronic Detection of SARS-CoV-2 Antibodies and Antigens at Attomolar Level

Yeji Choi[1,2], Seyedsina Mirjalili[1,2], MD Ashif Ikbal[1,2], Sean McClure[1], Scott Clemens[1], Jose Solano[1], John Heggland[1], Jiawei Zuo[1], and Chao Wang[1,2]*

[1]School of Electrical, Computer and Energy Engineering, Arizona State University, Tempe, AZ 85287, USA

[2]Biodesign Center for Molecular Design and Biomimetics, Arizona State University, Tempe, AZ 85287, USA

#Equal Contributions:

1- Yeji Choi

2- Seyedsina Mirjalili

***Corresponding Author: wangch@asu.edu**

1. Design and Configuration of the NasRED Housing and Tube Holder

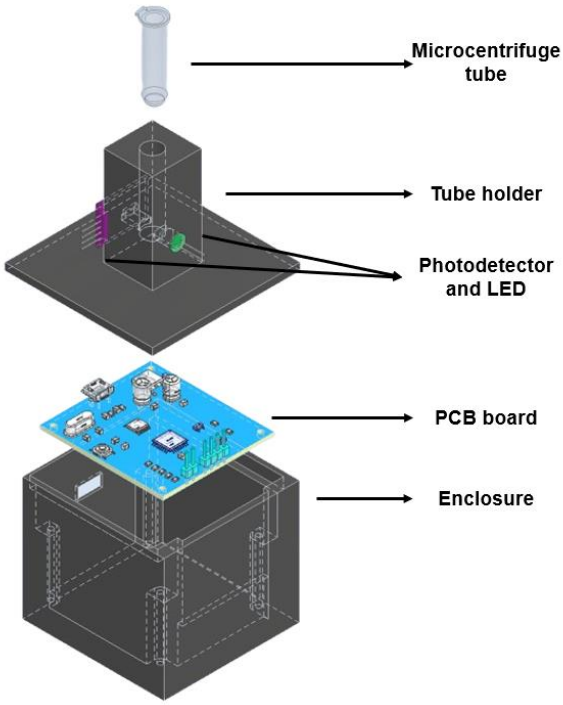

Supplementary Figure S1: Design and configuration of the NasRED readout system. Schematic diagram of the main architecture of the tube holder and housing box. The box had dimensions of 58 mm × 54 mm × 85 mm (length × width × height) and was printed using black carbon fiber polycarbonate filament to block the ambient light. The tube holder was designed to mount the LED and PD to measure the light intensity, and the light path was aligned to measure the supernatant in the microcentrifuge tube. The housing box was mechanically designed to host both the PCB board and the battery.

Table S1. Comprehensive breakdown of PED components and associated cost

Component	Qty (Unit)	Cost ($)	Total ($)
Microprocessor			
Atmega328	1	2.74	2.74
Capacitor (22 pF)	2	0.021	0.042
16MHz Crystal	1	0.346	0.346
Push switch	1	0.18	0.18
Resistor (1k Ohm)	1	0.024	0.024
Constant current LED driver circuit			
Resistor (1k Ohm)	1	0.024	0.048
Resistor (33 Ohm)	1	0.024	0.048

Green LED	1	0.1	0.1
BJT	2	0.074	0.148
Voltage regulator			
Electrolytic capacitor (10 μF)	2	0.162	0.324
Ceramic capacitor (0.1 μF)	2	0.038	0.076
Voltage regulator	1	0.404	0.404
Zener diode	1	0.172	0.172
Miscellaneous			
9V Battery	1	2.01	2.01
Tube holder	1	2.5	2.5
Photodetector	1	1.956	1.956
Custom PCB	1	9	9
		Device Total ($)	**20.07**

2. Comparison of voltage and current signals according to various circuit configurations

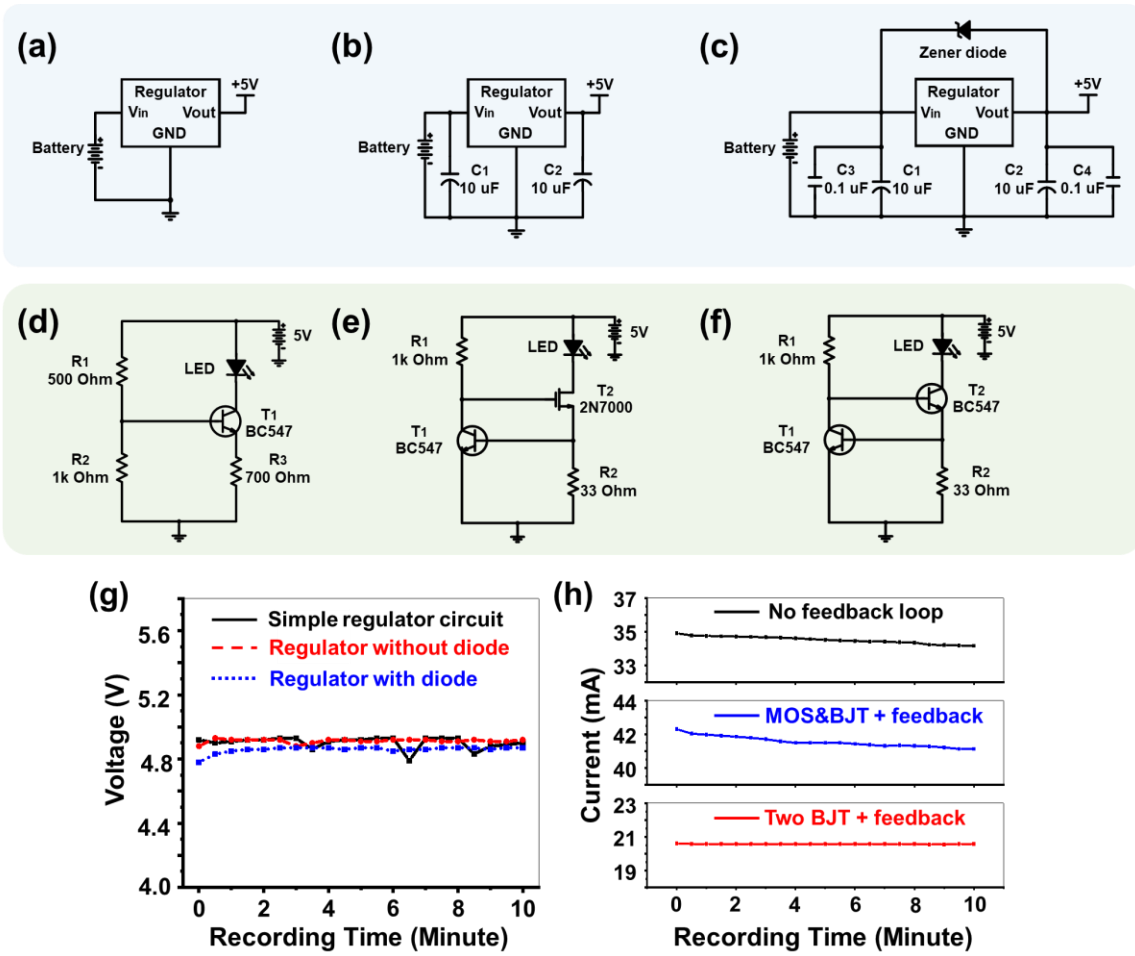

(i)

Constant current LED driver circuit	Capacitance (pF)	Resistance (Ohm)	Stabilization time (minute)
(d)	1.41	545.5	15
(e)	3.71	31.9	> 15
(f)	1.26	31.9	0.5

Supplementary Figure S2: Circuit design diagrams and their roles in signal stabilization. (a-c) The circuit diagrams show: (a) only a regulator, (b) the regulator connected to electrolytic capacitors to remove noise, and (c) the regulator connected to electrolytic capacitors, ceramic capacitors, and a Zener diode. The ceramic capacitor removed high-frequency noise to increase the stability of the circuit, and the Zener diode removed random noise spikes to provide an initial stable power supply. (d-f) The circuit diagram showing three constant current LED driver circuits: (d) one BJT without a feedback loop, (e) BJT and metal–oxide–semiconductor field-effect transistor (MOSFET) in a feedback loop, and (f) dual BJT in a feedback loop. (g) Stability of voltage signals for the three voltage regulator configurations, i.e. regulator only (black solid line), a regulator with electrolytic capacitors (red dash line), and a regulator with both capacitors and a Zener diode (blue dot line). (h) LED current values plotted for the three constant-current circuit configurations, i.e. without any feedback loop (black line), BJT-MOSFET feedback loop (blue

line), and double BJT feedback loop (red line). Indeed, the double-BJT feedback design had the smallest capacitance values (1.26 pF), resistance values (31.9 Ohm) and the most stable current. (i) A table summary of capacitance values and resistance values of the circuits for constant current LED. It was understood and observed that the current would drop in the absence of a feedback loop and that having a large capacitance and resistance would prolong the initiation time to reach a stable current. Unnecessary features, such as digital pins and a battery-powered device, were removed to minimize the chip size for printed circuit board (PCB) integration.

3. Analysis of the impact of operation protocol on electronic readout

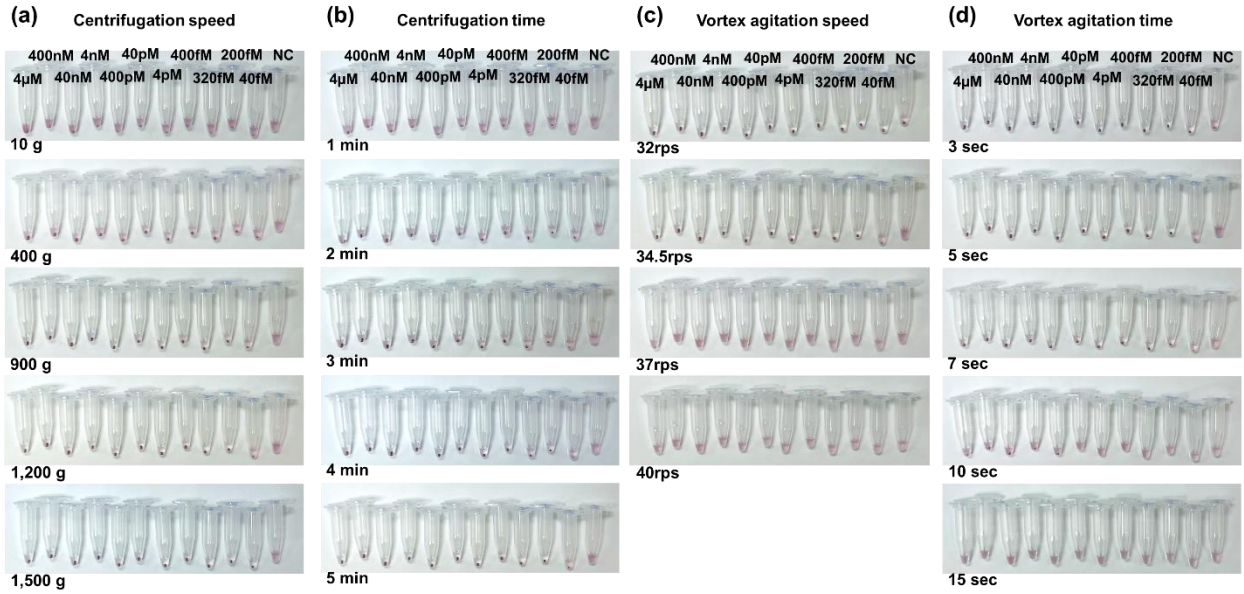

Supplementary Figure S3: Optical images of AS35 samples after various device protocol conditions: (a) The centrifuge speed was increased from 10 g to 1,500 g for 5 minutes. The other parameters were: post-centrifugation incubation for 5 minutes and vortex agitation at 34.5 rounds per second (rps) for 5 seconds. (b) The centrifugation time was increased from 1 min to 5 min at 1,200 g of speed. The other parameters included: incubation at 5 min and vortex agitation at 34.5 rps for 5 seconds. (c) The vortex agitation speed was increased from 32 rps to 40 rps for 5 seconds. The other parameters were: centrifugation at 1,200 g for 5 minutes and incubation for 5 minutes. (d) The vortex agitation time was increased from 3 seconds to 15 seconds at 34.5 rps of speed. The other parameters were: centrifugation at 1,200 g for 5 minutes and incubation at 5 minutes.

4. AuNP Quantification Analysis

4.1 AuNP concentration measurement

Using 80 nm streptavidin-functionalized AuNPs as a model, we attempted to determine the AuNP concentration C_{AuNP} (#/mL). The purchased AuNPs (Cytodiagnostics) had an initial optical density (OD) of 10 reported by the manufacturer. OD is a value that indicates the degree to which

light is absorbed to measure concentration or quantity. Here, OD is defined as the decadic logarithm (base 10) of the ratio of incident to transmitted optical power, and a higher OD means a large extinction and a high AuNP concentration. However, a precise determination of their concentration C_{AuNP} was not available from the manufacturer. For NanoSight (NS300, Malvern Panalytical) measurements, the as-purchased AuNP solutions were diluted three folds, and then serially diluted with a 1.5-fold dilution factor.

To correlate the Nanosight signals with PED signals, 24 µL of AuNPs solutions at each concentration were added to each microcentrifuge tube and measured using NasRED.

Here, C_{AuNP} was obtained from NanoSight and fitted to the manufacturer's OD using a linear equation (1) as follows:

$$C_{AuNP} = 1.89 \times 10^6 OD + 5.81 \times 10^7 \qquad (1)$$

Further, the optical extinction signal obtained from NasRED readout OD_{PED} was also fitted to the manufacturer's OD values with a linear relation as follows:

$$OD_{PED} = 0.3OD + 0.06 \qquad (2)$$

The above equations can be used to determine the C_{AuNP} concentrations at the electronic signals of the NasRED using a simple linear relationship.

$$C_{AuNP} = 6.3 \times 10^6 \times OD_{PED} + 5.77 \times 10^7 \quad (3)$$

Using equation (3), the relationship can also be plotted (Fig. S5 e), which can be used to calibrate the AuNP numbers for each measured electronic signal intensity value.

Here, the averaged PBS buffer sample signals, $T(PBS) = \frac{\sum_i (T_i(PBS))}{5}$ (i=1 to 5 for the five measurements), represented the optical transmission through each tube containing 24 µL of PBS buffer. Similarly, for the diluted AuNPs, five measurements were performed for each tube along the same orientations, and the electronic signals were again recorded as $T(C_{AuNP}) = \frac{\sum_i (T_i(C_{AuNP}))}{5}$ (i=1 to 5, at AuNP concentration C_{AuNP}). $OD_{PED}(C_{AuNP})$ is calculated to correlate the AuNP concentrations with the PED measured signals following:

$$OD_{PED}(C_{AuNP}) = \frac{T(PBS) - T(C_{AuNP})}{T(PBS)} = 1 - \frac{T(C_{AuNP})}{T(PBS)} \quad (4)$$

$$\text{Or } C_{AuNP} = 6.3 \times 10^6 \times \left(1 - \frac{T(C_{AuNP}(C))}{T(PBS)}\right) + 5.77 \times 10^7 \ (5)$$

4.2 PED signal correlation

As detailed in the Method section, S_{PED} is a function of the tested protein marker concentration C, and normalized against the transmission signals $T(PC)$ and $T_0(NC)$ from a positive control (PC) and negative control (NC) sample, following:

$$S_{PED}(C) = \frac{T(PC) - T_0(NC) - T_D(C) + T_D(NC)}{T(PC) - T_0(NC)} = \frac{T(PC) - T_t(C) + T_0(C) - T_0(NC) + T_D(NC)}{T(PC) - T_0(NC)} \qquad (6)$$

Here, $T(PC) \cong T(PBS) \cong 196$ (arbitrary units from PED readout) is the highest possible optical transmission for a given test in PBS, and $T_0(C) = T_0(NC) \cong 111$ is the transmission of the AuNP solution after mixing (thus irrelevant to the protein concentration), $T_t(C)$ is the

transmission of a possible protein sample after test, and $T_D(NC) \cong 0$ is the transmission signal difference after and before the sensing protocol for the negative control . Therefore, we can write:

$$S_{PED}(C) = \frac{196 - T_t(C)}{85}, \text{ or } T_t(C) = 196 - 85 S_{PED}(C) \qquad (7)$$

Effectively, in our experiment, we diluted the AuNP sensors to a target concentration of about OD~0.5. To correlate the OD_{PED} with S_{PED}, we should have $T(C_{AuNP}(NC)) = T_t(NC)$, and $S_{PED}(NC) = 1$. Mathematically from (4) and using our experimental values for $T_t(NC)$ and $T(PC)$, we can obtain $OD_{PED} = 1 - \frac{T_t(NC)}{T(PC)} \cong 1 - 0.57 = 0.43$. This is indeed close to the targeted 0.5 OD value.

On the other hand, when a particular diluted AuNP solution at concentration C_{AuNP} displays the same color as a AuNP sensor solution after protein test at a protein concentration *C*, we then have that $T(C_{AuNP}(C)) = T_t(C)$, and we can relate the AuNP concentration with the S_{PED} signal as:

$$C_{AuNP} = 6.4 \times 10^7 - 3.2 \times 10^4 \times T_t(C) = 6.4 \times 10^7 - 6.3 \times 10^6 + 2.7 \times 10^6 \times S_{PED}(C)$$
$$= 2.7 \times 10^6 \times S_{PED}(C) + 5.7 \times 10^7 \qquad (8)$$

This further allows us to estimate the amount remaining free-floating AuNPs after a test from the S_{PED} signal. While the accuracy of AuNP concentration could be limited by the NanoSight precision and human errors in sample dilution, this analysis demonstrated that the AuNP concentration is linearly correlated with the S_{PED} values.

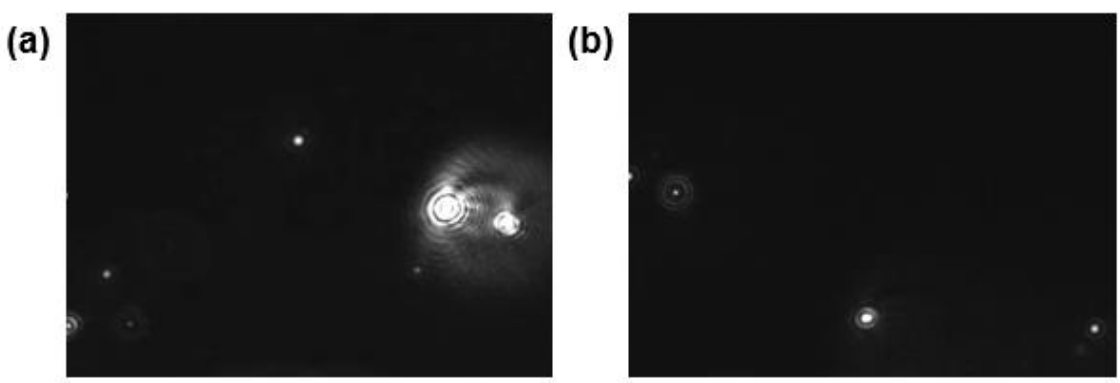

Supplementary Figure S4: Optical images of exemplary 80 nm streptavidin functionalized AuNPs using NanoSight. (a) AuNPs diluted 3-fold from the stock concentration, and (b) AuNPs further diluted 1.5-fold from (a). A consistent decrease in the number of particles was observed after each dilution.

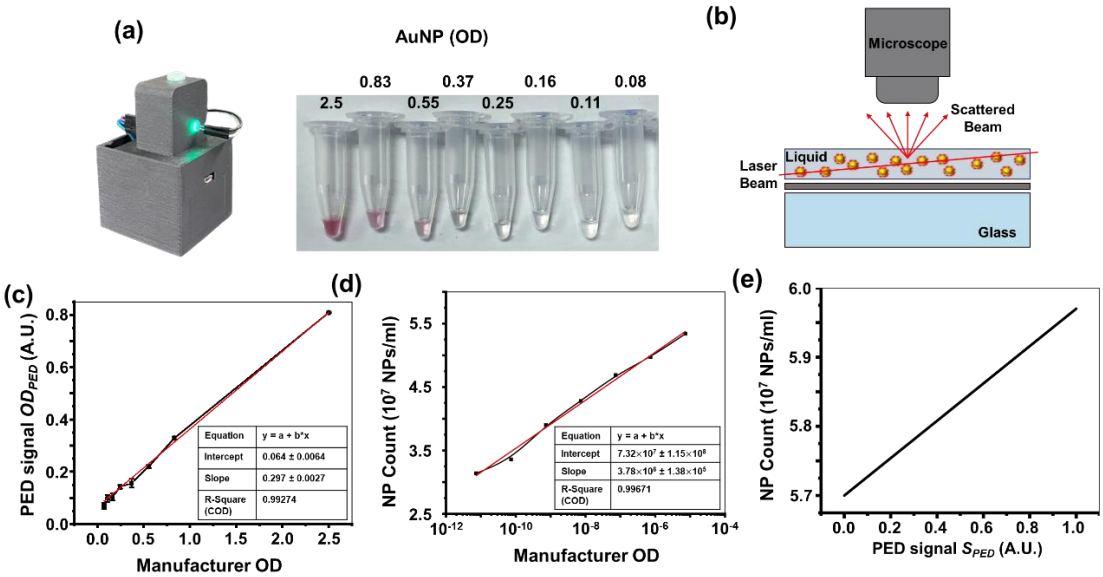

Supplementary Figure S5: Analysis of nanoparticle concentrations. (a) Tube pictures showing the change of AuNP solution color at various dilutions correlated with the OD from manufacturer. (b) Schematics of the Nanosight apparatus where the pattern of the scattered beam through the solution was analyzed to yield the number of particles in liquid. (c) The electronic readout signal S_{PED} plotted against manufacturer-provided OD values. (d) The nanoparticle concentration measured by NanoSight plotted against manufacturer-provided OD values. (e) Extracted nanoparticle concentration plotted against the normalized electronic readout signals S_{PED} from NasRED.

5. TEM imaging of AuNP precipitates

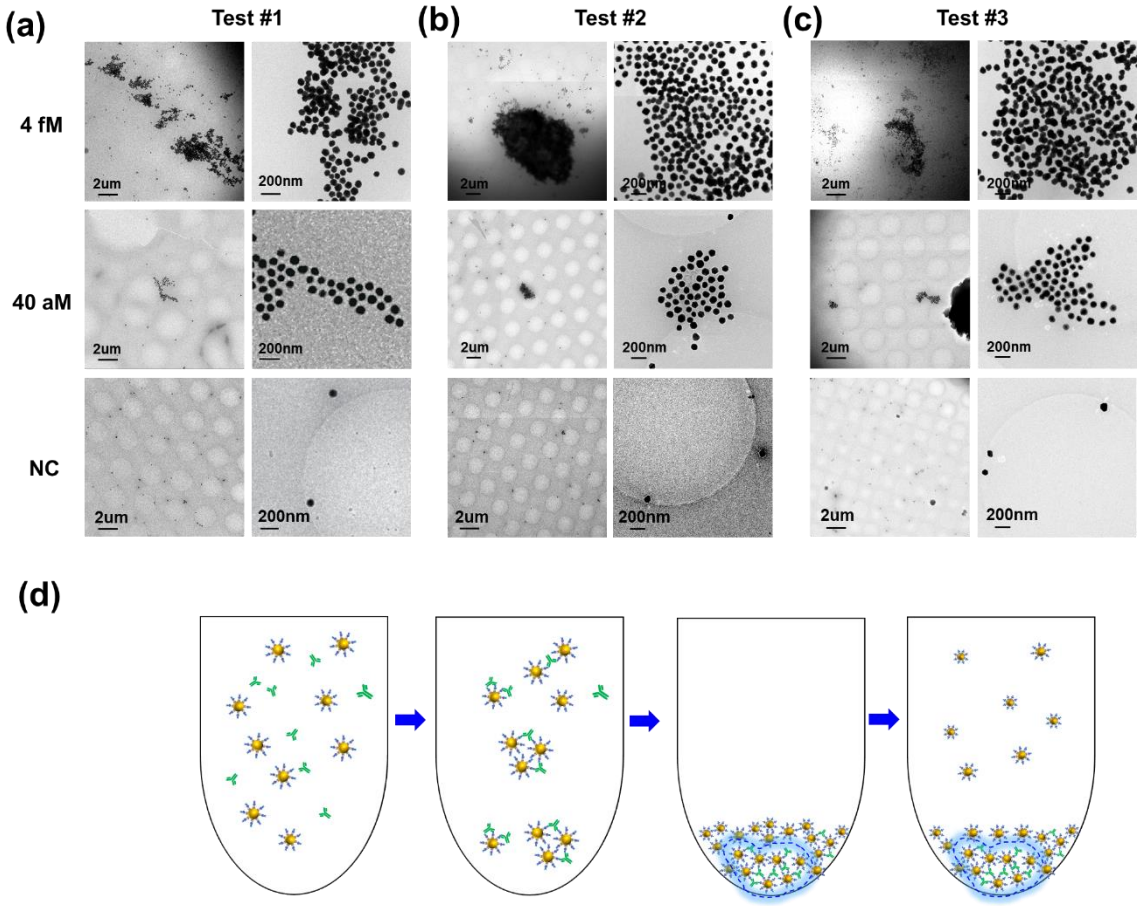

Figure S6. Microscopy analysis of AuNP precipitates. (a-c) Cryo-TEM images of 80 nm AuNP precipitates at the tube bottom in three replicate experiments at different AS35 concentrations (4 fM, 40 aM, and NC from top to bottom rows). (d) Schematic representations of the AuNP cluster formation and precipitation mechanism during sensing process: (i) a uniform mixing of AuNPs with target proteins, (ii) AuNP sensors react to and bind to target proteins, thus forming clusters, during centrifugation, (iii) after centrifugation and during incubation, the AuNP clusters form precipitates at the tube bottom, and (iv) vortex agitation releases loose AuNPs back into the solution. It is also hypothesized that the eventual precipitates of AuNPs consist of protein-induced large AuNP clusters as well as small AuNP oligomers or monomers that formed around such clusters. The large AuNP clusters are attributed to the biochemical interactions between proteins and antibodies. Such large clusters can physically trap small AuNP monomers or oligomers by interrupting fluidic flow during centrifugation and vortex agitation. Or such AuNP clusters, with highly concentrated proteins and antibodies, could greatly modulate the charge distribution around them, and thus electrostatically attract additional AuNPs. Future theoretical and empirical studies are needed to understand the mechanisms comprehensively.

6. Sensing optimizations of SARS-CoV-2 antibody and antigen

6.1 SARS-CoV-2 antibody detection in sera and blood

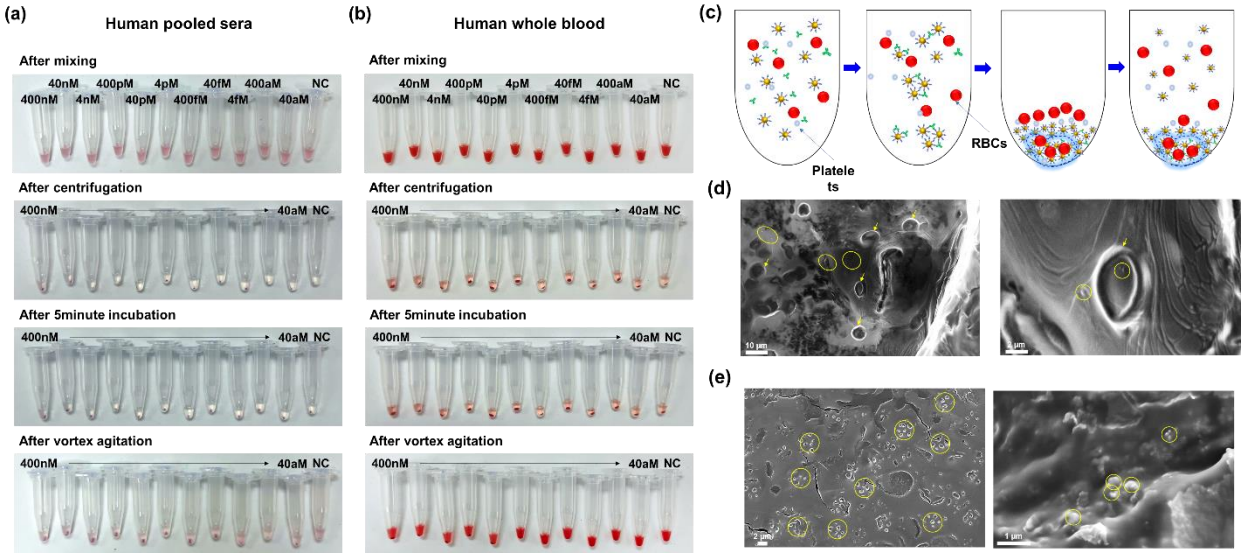

Supplementary Figure S7: Extended data of microcentrifuge tubes used for SARS-CoV-2 antibody detection. (a-b) Images of centrifuge tubes for AS35 antibody detection in: (a) human pooled serum samples, (b) human whole blood. Immediately after mixing the sensor solutions in all tubes had identical and homogenous colors. Then, functionalized AuNPs precipitated after the centrifugation and incubation in the sera samples, while both AuNPs and blood cells precipitated in blood. After vortex agitation, the unbound free-floating AuNPs and blood cells were dispersed for both sera and blood samples, but the AuNP clusters stayed at the tube bottom. The clusters could also have included blood cells and platelets co-precipitated with AuNPs at the bottom of the tube. (c) Conceptual representation of the co-precipitation mechanism. (d-e) SEM images of the NC sample in blood matrix. (d) (left) NC samples showing blood cell (yellow arrows) and AuNPs (yellow circles) distributed on the imaging grid. (right) Zoomed-in image showing a red blood cell with AuNPs, indicating the possibility of AuNP uptake. (e) The sample with 40 fM antibody concentration, showing the AuNPs in the biological matrix, with a possibility that the AuNPs caused lysis of the blood cells. These SEM results indicated the complexity of AuNP interactions with blood cells during centrifugation, incubation, and vortex agitation, which could include cell uptake of individual AuNPs, AuNP cluster formation at the presence of complex biological matrix, cell lysis, etc. Future theoretical and empirical studies are needed to understand the mechanisms comprehensively.

6.2 SARS-CoV-2 antibody detection in human whole blood sample using different sensing protocols

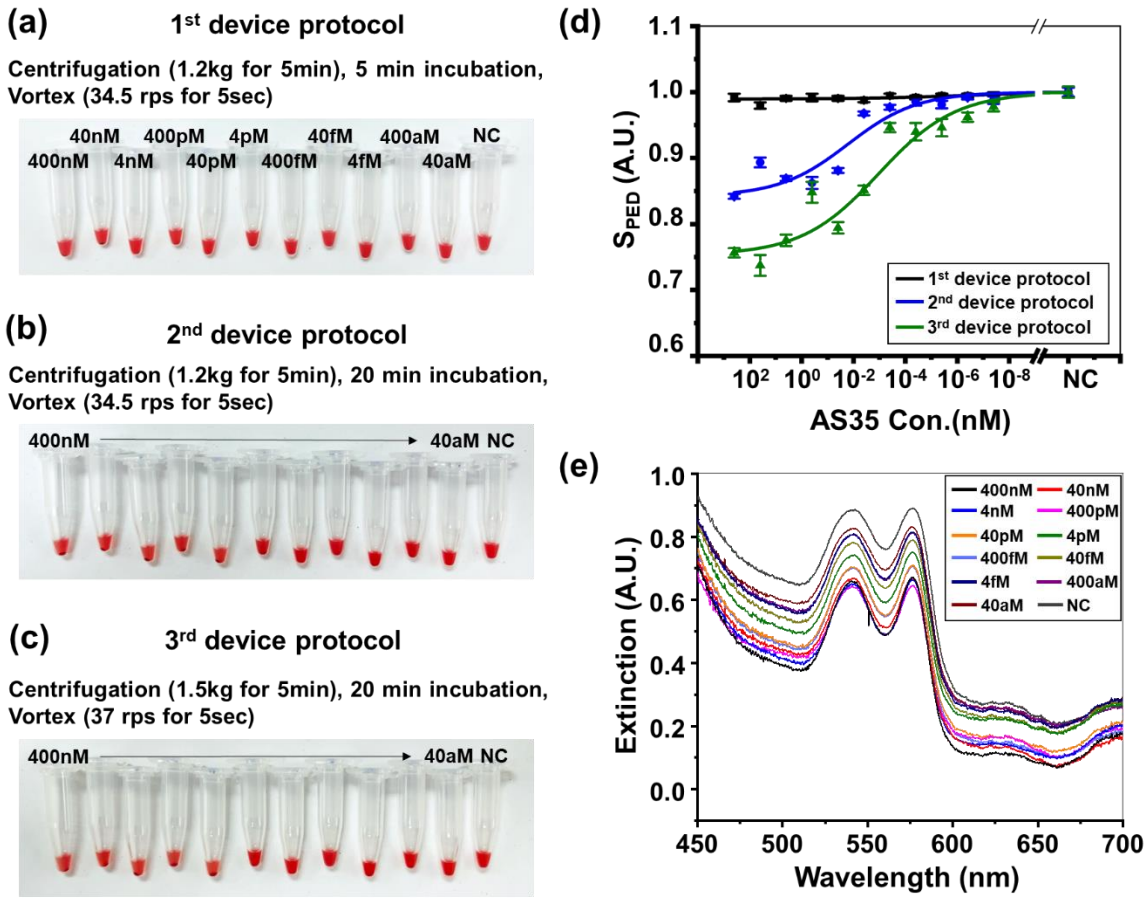

Supplementary Figure S8: Experimental demonstrations of SARS-CoV-2 antibody detection in 20% diluted human whole blood following different sensing protocols (Table S2). (a-c) Optical images showing spiked antibody in WB samples ready for NasRED readout. Clearly, more visible AuNP clusters were observed at the tube bottoms under protocols #2 and #3. (d) Extracted PED signals plotted against antibody concentration using the three sensing protocols. (e) The optical extinction signals spectra measured by a spectrometer in the visible range (450 - 700 nm) for antibody samples analyzed following the 3rd protocol. Here the supernatants of blood samples were loaded from the tubes into a PDMS plate for spectrometer measurement.

Table S2. Parameters in WB sensing protocols

Protocol	**# 1**	**# 2**	**#3**
Centrifugation	1200 ×g; 5 min	1200 ×g; 5 min	1500 ×g; 5 min
Incubation	5 min	20 min	20 min
Vortex	~2100 rpm, 5 sec	~2100 rpm, 5 sec	~2250 rpm, 5 sec

6.3 Reproducibility test of SARS-CoV-2 antibody detection in PBS and WB and data analysis

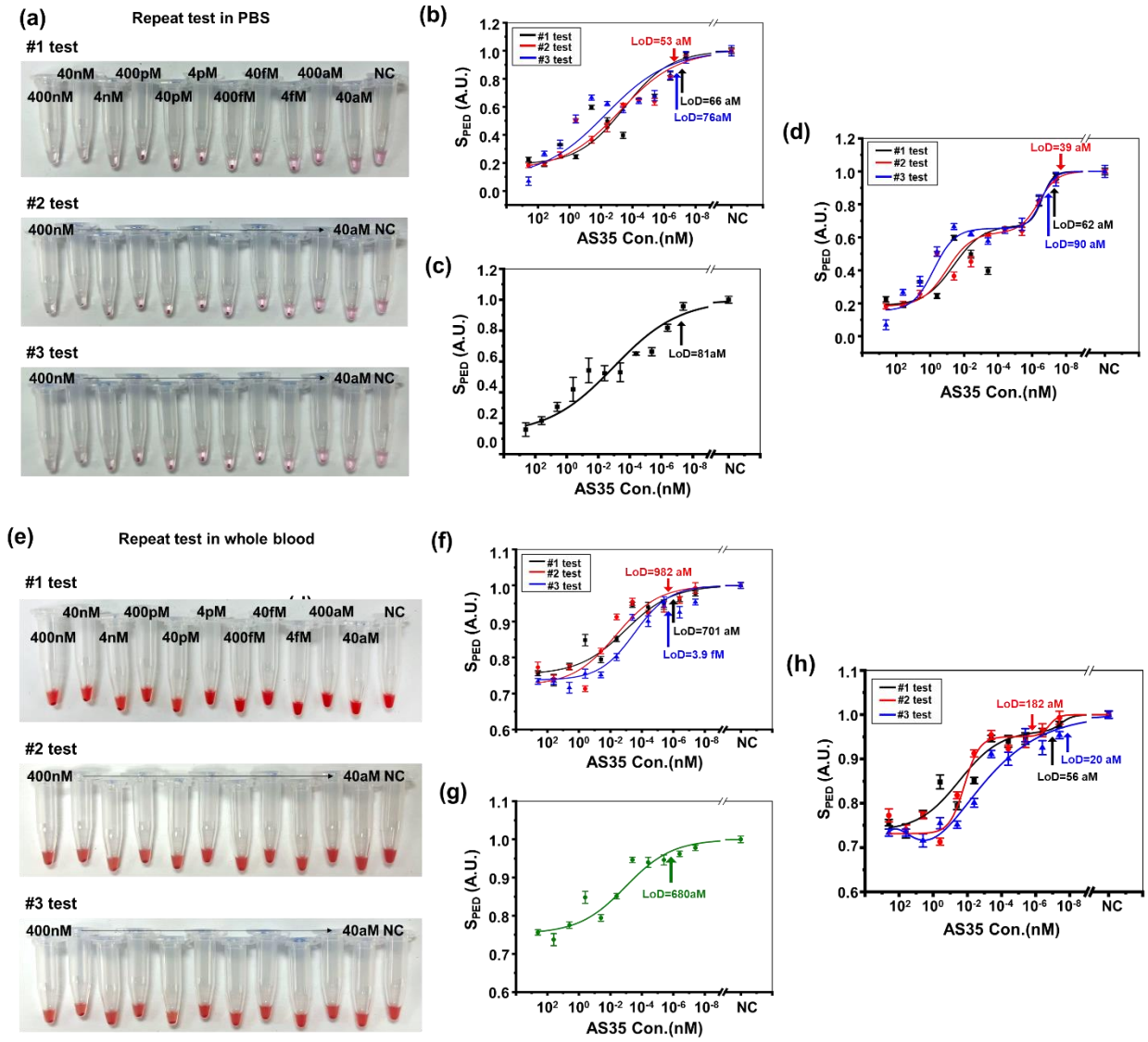

Supplementary Figure S9: Reproducibility test of antibody in PBS and WB. (a-d) Tests in PBS: (a) Optical images of microcentrifuge tubes in 3 individual replicates ready for readout, (b) Extracted PED signals and sigmoidal-fitted response curves for the three replicates, producing an LoD of 66, 76, and 53 aM, respectively, (c) Averaged signals of the 3 replicate experiments in PBS, with an LoD of 81 aM, and (d) biphasic dose response fitting that yielded an LoD of 32, 62, and 90 aM, respectively. (e-h) Tests in 20% WB: (e) Optical images of testing tubes in 3 replicates, (f) Extracted PED signals and sigmoidal-fitted responses yielding an LoD of 0.7, 3.9, and 0.1 fM, respectively, (g) Averaged signals of the 3 replicate experiments in WB with a LoD of 680 aM, and (h) Biphasic dose response fitting of data showing LoDs of 182, 20, and 56 aM, respectively. Interestingly, the 3 replicates in PBS revealed a small standard deviation (<3%) of S_{PED} at low concentrations (40 fM - 40 aM) but higher deviations (20 to 30%) at intermediate concentrations (400 pM - 400 fM). Counterintuitively, the three replicates in WB samples showed more consistent readout signals (deviation of <9%) across all concentrations. Also, it has been observed the

biphasic does response model provides better LoD values and goodness of fit, which calls for further exploration to explain the underlying mechanisms of biochemical and fluid dynamic interactions. The consistency of fits for the three sets shows the high reproducibility of the proposed sensor platform. Error bars represent the standard deviations of measurements within each set. For consistency, we only used the sigmoidal fitting-derived LoDs in this paper when comparing NasRED to other technologies, despite that biphasic response provided better fitting and better LoDs.

7. Quantitative Polymerase Chain Reaction (qPCR) response settings and conditions

In our qPCR protocol for SARS-CoV-2 RNA, the temperature was set to 50°C for 2 minutes for the reverse transcription step to convert the RNA into complementary DNA (cDNA). This was followed by an initial denaturation step at 95°C for 20 seconds to separate the double-stranded cDNA into single strands. Then, during a thermocycling step that repeated for 40 times, the temperature was maintained at 95°C for 3 seconds and then at 60°C for 30 seconds for the annealing and extension step, where primers (Table S3) specific to N-protein coding gene bonded to the cDNA and new DNA strands were synthesized.

To quantify the concentrations of the PROtrol sample, the samples were diluted, tested in triplicate and each repeated in two separate runs. The undiluted sample (nt) had an average cycle threshold (Ct) value of 12.57, corresponding to a concentration of 1.57×10^9 copies/mL. However, given the high testing concentration, the nt values were only used as a reference but excluded from the calculation of virion particle concentrations to prevent skewing of the data. The 1:10 dilution had an average Ct value of 14.68, translating to a concentration of 4.92×10^9 copies/mL for undiluted sample. The 1:100 dilution sample resulted in an average Ct value of 17.83, i.e. a concentration of 2.35×10^9copies/mL for the undiluted sample. Further, the 1:1000 dilution yielded an average Ct value of 21.22, or a concentration of 5.23×10^9copies/mL for the undiluted sample. The positive extraction control had a Ct value of 24.97, while the positive plate control had a Ct value of 26.42. The no-template control (water) showed an 'Undetermined' Ct value, indicating no contamination in the reagents used.

The standard curve generated from the in-house standard samples showed a slope of -3.492, an efficiency of 93.376%, and an R-squared value of 1.00, indicating a highly efficient and reliable qPCR assay.

Table S3. DNA Sequence of Primer and Probe for qPCR Reaction.

Primers & Probe	Primer / Probe Sequence (5' — 3')
Z2020-01-Fwd	CTG ATG CTG CTC TTG CTT TG
Z2020-01-Rev	GTG ACA GTT TGG CCT TGT TG
Z2020-01-Prb	TCA CAG ATT GAA CCA GCT TGA GAG CA

Table S4. Inactive virus sample summary of initial and NaSRED test concentrations

Assay/Measured	Initial Concentration	Initial Volume (µl)	Triton X-100 Volume (µl)	Final Volume (µl)	Final test Concentration
ELISA/N-protein	60.5 nM	10	10	20	30.03 nM
	2995 ng/mL	10	10	20	1500 ng/mL
qPCR	4.69×10^9 copies/mL	10	10	20	2.35×10^9 copies/mL
Culture	2.73×10^7 TCID50/mL	10	10	20	1.737×10^7 TCID50/mL

8. Comparison of NasRED with representative diagnostic technologies

Table S5. Competing Diagnostic Approaches for SARS-CoV-2 Detection: Commercial methods of LFA

Test name	LoD (ng/mL)	LoD (TCID50/mL)	Detection time (min)	Testing cost	Ref.
Flowflex COVID-19 Antigen Home Test	0.3	3.57×10^3	15-30	~$8	[1]
Genabio COVID-19 Rapid Self-Test kit	2.12	2.52×10^4	15	~$12	[2]
iHealth COVID-19 Antigen Rapid Test	2.38	2.83×10^4	15	~$10	[3]
Panbio COVID19 Ag Rapid Test Device	0.019	2.26×10^2	15	~$12	[4]
Fastep COVID-19 Antigen Home Test	0.033	3.93×10^2	15	~$3	[5]
NasRED	0.00002	0.24	15-30	~$2	This Work

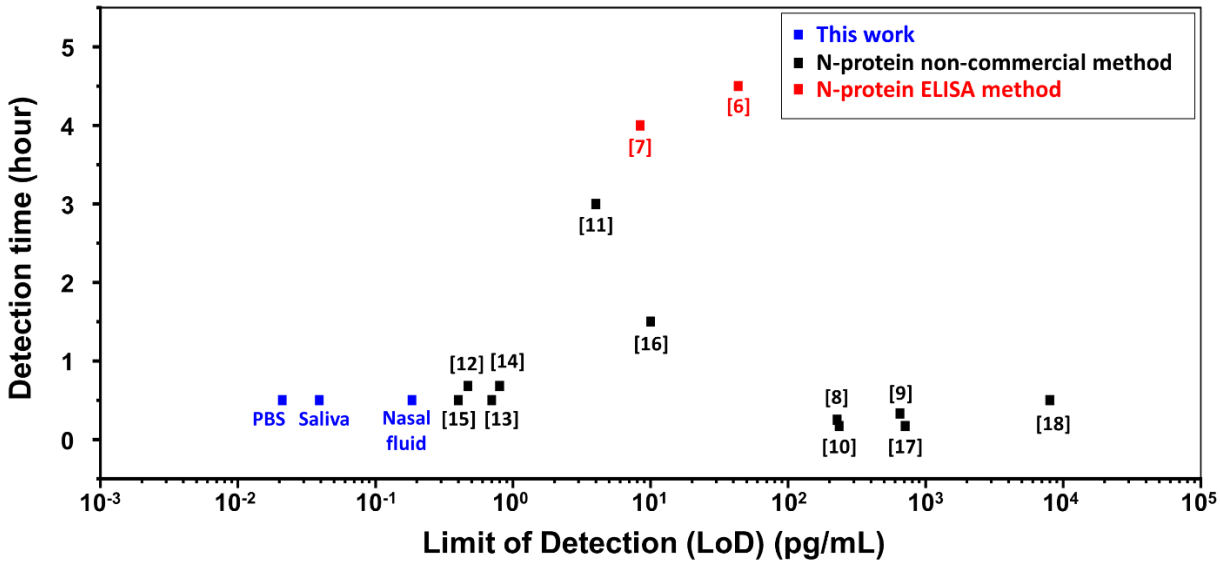

Supplementary Figure S10: Assay LoD and time comparison. NasRED presented a low LoD and short detection time, both the best among the various methods examined in this study.

Table S6. Competing Diagnostic Approaches for SARS-CoV-2 N-Protein Detection: A Review of Peer-Reviewed Literature

Method	LoD (pg/mL)	Sample volume (µL)	Medium	Detection time	Ref.
ELISA	43.3	5 – 100	Nasopharyngeal	4.5 hours	[6]
ELISA	8.4	5 – 100	Nasopharyngeal	4 hours	[7]
Electrochemical sensor	227	30	Saliva	15 min	[8]
LFA	650	75	PBS	20 min	[9]
LFA	235	100	Spike saliva	10 min	[10]
SPR sensing	4	-	PBS	> 3 hours	[11]
Electrochemical sensor	0.47	60	Serum	40 min	[12]
Electrochemical sensor	0.7	-	Nasopharyngeal	30 min	[13]
Electrochemical sensor	0.8	100	Spike Nasopharyngeal	40 min	[14]

Electrochemical sensor	0.4	20	Nasopharyngeal	30 min	[15]
Microcantilever-based optical detection	10	50	Serum	1.5 hours	[16]
Electrochemical sensor	710	-	Nasopharyngeal	10 min	[17]
Electrochemical sensor	$8x10^3$	300	Saliva, Nasopharyngeal	30 min	[18]
NasRED	0.021 0.039 0.184	8	PBS Spike saliva Spike Nasal fluid	15 to 30 min	This work

Note: The NasRED sensitivity is 6,000 times better than LFA in saliva (21) and 31,000 times better in PBS (20), and 45 or ~230 times better than ELISA (16,17).

Table S7. Competing Diagnostic Approaches for SARS-CoV-2 Detection: Commercial methods of PCR

Manufacturer and instrument	**LoD (copies/mL)**	**Time-to-result**	**Sample volume (µL)**	**Size (width x height x depth, cm^3) and weight (kg)**	**Instrument Cost**	**Ref.**
Roche, Cobas 6800	250	3.5 hours	400	292x222x129, 1624kg	~$20,000	[19]
Abbott, ID NOW	10^5	15 min	200	20x14x19, 3kg	~$12,000	[20]
Abbott, M2000	100	5 hours	250	145x217x79, 314kg	~$100,000	[21]
Hologic, Panther	600	2.4 hours	25	193x175x81, 363kg	~$80,000	[22]
DiaSorin, Simplexa	500	1.5 hours	50	30x30x20, 30kg	~$40,000	[23]
Roche, GenMark ePlex	10^6	1.5 hours	200	54x59x48, 49kg	~$20,000	[24]

Roche, LightCycler 480	785	40 min	10-50	57x50x59, 56kg	~$15,000	[25]
Thermo Fisher, QuanStduio™ 5	350	30 min	20	27x40x50, 26kg	~$55,000	[26]
BIO RAD, CFX96 Dx	250	30 min	10-25	33x36x46, 21kg	~$12,000	[27]
Thermo fisher, Applied Biosystems 7500 Fast Dx	250	40 min	10-30	34x49x45, 34kg	~$12,000	[27]
NasRED	32*	15 to 30 min	8	5.8x5.4x8.5, <1kg **	~$20	This work
				35x36x25, <15kg ***	~$3,000	

*Note: 32 copies/mL when fitted with single-dose response curve, and 0.13 when fitted with biphasic-dose response curves.

** The PED reader itself weighs only 125 grams.

*** The weight included the centrifuge, vortexer, and the PED reader. The centrifuge weighs 10 kg, and the vortex weighs 4.5kg.

Reference

(1) Flowflex. *Flowflex COVID-19 antigen rapid test package insert*. https://flowflexcovid.com/ (accessed 2024-08-16).

(2) Genabio. *Genabio COVID-19 rapid self-test kit*. https://www.genabio.com/covid/ (accessed 2024-08-16).

(3) iHealth. *iHealth COVID-19 antigen rapid test*. https://ihealthlabs.com/products/ihealth-covid-19-antigen-rapid-test?srsltid=AfmBOopp4Xjzv-uEyn7R7XCppH7XUWWWm0S3PSYqq57E2ldIP8bumQRS (accessed 2024-08-16).

(4) Abbott. *Panbio COVID-19 antigen rapid test device*. https://www.globalpointofcare.abbott/gb/en/product-details/panbio-covid-19-ag-antigen-test.html (accessed 2024-08-16).

(5) Biotech Inc, A. *Fastep COVID-19 antigen home test - instructions for use healthcare provider*. https://www.fda.gov/media/163447 (accessed 2024-08-16).

(6) Yadegari, H.; Mohammadi, M.; Maghsood, F.; Ghorbani, A.; Bahadori, T.; Golsaz-Shirazi, F.; Zarnani, A. H.; Salimi, V.; Jeddi-Tehrani, M.; Amiri, M. M.; Shokri, F. Diagnostic Performance of a Novel Antigen-Capture ELISA for the Detection of SARS-CoV-2. *Anal Biochem* **2023**, *666*, 115079. https://doi.org/10.1016/j.ab.2023.115079.

(7) Humbert, M. V.; Opurum, P. C.; Brendish, N. J.; Poole, S.; He, P.; Katis, I.; Quaye, J.; Bediako, Y.; Duriez, P. J.; Eason, R. W.; Sones, C.; Quaye, O.; Awandare, G. A.; Christodoulides, M.; Clark, T. W.; Quashie, P. K.; McCormick, C. J. A SARS-CoV-2 Nucleocapsid ELISA Represents a Low-Cost Alternative to Lateral Flow Testing for Community Screening in LMI Countries. *Journal of Infection* **2022**, *84* (1), 48–55. https://doi.org/10.1016/j.jinf.2021.08.049.

(8) Białobrzeska, W.; Ficek, M.; Dec, B.; Osella, S.; Trzaskowski, B.; Jaramillo-Botero, A.; Pierpaoli, M.; Rycewicz, M.; Dashkevich, Y.; Łęga, T.; Malinowska, N.; Cebula, Z.; Bigus, D.; Firganek, D.; Bięga, E.; Dziąbowska, K.; Brodowski, M.; Kowalski, M.; Panasiuk, M.; Gromadzka, B.; Żołędowska, S.; Nidzworski, D.; Pyrć, K.; Goddard, W. A.; Bogdanowicz, R. Performance of Electrochemical Immunoassays for Clinical Diagnostics of SARS-CoV-2 Based on Selective Nucleocapsid N Protein Detection: Boron-Doped Diamond, Gold and Glassy Carbon Evaluation. *Biosens Bioelectron* **2022**, *209*, 114222. https://doi.org/10.1016/j.bios.2022.114222.

(9) Grant, B. D.; Anderson, C. E.; Williford, J. R.; Alonzo, L. F.; Glukhova, V. A.; Boyle, D. S.; Weigl, B. H.; Nichols, K. P. SARS-CoV-2 Coronavirus Nucleocapsid Antigen-Detecting Half-Strip Lateral Flow Assay toward the Development of Point of Care Tests Using Commercially Available Reagents. *Anal Chem* **2020**, *92* (16), 11305–11309. https://doi.org/10.1021/acs.analchem.0c01975.

(10) Xie, Z.; Feng, S.; Pei, F.; Xia, M.; Hao, Q.; Liu, B.; Tong, Z.; Wang, J.; Lei, W.; Mu, X. Magnetic/Fluorescent Dual-Modal Lateral Flow Immunoassay Based on Multifunctional Nanobeads for Rapid and Accurate SARS-CoV-2 Nucleocapsid Protein Detection. *Anal Chim Acta* **2022**, *1233*, 340486. https://doi.org/10.1016/j.aca.2022.340486.

(11) Yano, T. aki; Kajisa, T.; Ono, M.; Miyasaka, Y.; Hasegawa, Y.; Saito, A.; Otsuka, K.; Sakane, A.; Sasaki, T.; Yasutomo, K.; Hamajima, R.; Kanai, Y.; Kobayashi, T.; Matsuura, Y.; Itonaga, M.; Yasui, T. Ultrasensitive Detection of SARS-CoV-2 Nucleocapsid Protein Using Large Gold Nanoparticle-Enhanced Surface Plasmon Resonance. *Sci Rep* **2022**, *12* (1), 1060. https://doi.org/10.1038/s41598-022-05036-x.

(12) Nie, W.; Zhang, R.; Hu, C.; Jin, T.; Wei, X.; Cui, H. A Self-Enhanced Electrochemiluminescence Array Chip for Portable Label-Free Detection of SARS-CoV-2 Nucleocapsid Protein with Smartphone. *Biosens Bioelectron* **2023**, *240*, 115662. https://doi.org/10.1016/j.bios.2023.115662.

(13) Raziq, A.; Kidakova, A.; Boroznjak, R.; Reut, J.; Öpik, A.; Syritski, V. Development of a Portable MIP-Based Electrochemical Sensor for Detection of SARS-CoV-2 Antigen. *Biosens Bioelectron* **2021**, *178*, 113029. https://doi.org/10.1016/j.bios.2021.113029.

(14) Eissa, S.; Zourob, M. Development of a Low-Cost Cotton-Tipped Electrochemical Immunosensor for the Detection of SARS-CoV-2. *Anal Chem* **2021**, *93* (3), 1826–1833. https://doi.org/10.1021/acs.analchem.0c04719.

(15) Eissa, S.; Alhadrami, H. A.; Al-Mozaini, M.; Hassan, A. M.; Zourob, M. Voltammetric-Based Immunosensor for the Detection of SARS-CoV-2 Nucleocapsid Antigen. *Microchimica Acta* **2021**, *188* (6), 199. https://doi.org/10.1007/s00604-021-04867-1.

(16) Li, J.; Lillehoj, P. B. Microfluidic Magneto Immunosensor for Rapid, High Sensitivity Measurements of SARS-CoV-2 Nucleocapsid Protein in Serum. *ACS Sens* **2021**, *6* (3), 1270–1278. https://doi.org/10.1021/acssensors.0c02561.

(17) Agarwal, D. K.; Nandwana, V.; Henrich, S. E.; Josyula, V. P. V. N.; Thaxton, C. S.; Qi, C.; Simons, L. M.; Hultquist, J. F.; Ozer, E. A.; Shekhawat, G. S.; Dravid, V. P. Highly Sensitive and Ultra-Rapid Antigen-Based Detection of SARS-CoV-2 Using Nanomechanical Sensor Platform. *Biosens Bioelectron* **2022**, *195*, 113647. https://doi.org/10.1016/j.bios.2021.113647.

(18) Fabiani, L.; Saroglia, M.; Galatà, G.; De Santis, R.; Fillo, S.; Luca, V.; Faggioni, G.; D'Amore, N.; Regalbuto, E.; Salvatori, P.; Terova, G.; Moscone, D.; Lista, F.; Arduini, F. Magnetic Beads Combined with Carbon Black-Based Screen-Printed Electrodes for COVID-19: A Reliable and Miniaturized Electrochemical Immunosensor for SARS-CoV-2 Detection in Saliva. *Biosens Bioelectron* **2021**, *171*, 112686. https://doi.org/10.1016/j.bios.2020.112686.

(19) Roche. *SARS-CoV-2 qualitative and quantitative assay for use on the cobas 6800 Systems*. https://www.fda.gov/media/159276 (accessed 2024-08-16).

(20) Abbott. *ID NOW COVID-19 2.0 assay*. https://www.globalpointofcare.abbott/us/en/product-details/id-now-covid-19-us.html (accessed 2024-08-16).

(21) Abbott. *Abbott m2000 real-time*. https://www.molecular.abbott/us/en/products/infectious-disease/RealTime-SARS-CoV-2-Assay (accessed 2024-08-16).

(22) Hologic; Inc. *Aptima® SARS-CoV-2 assay (Hologic Panther® System)*. https://www.fda.gov/media/138096 (accessed 2024-08-16).

(23) Viviani, T. *DiaSorin Simplex COVID-19 direct*. https://us.diasorin.com/en/molecular-diagnostics/kits-reagents/simplexa-covid-19-flu-ab-direct (accessed 2024-08-16).

(24) Roche. *GenMark ePlex SARS-CoV-2 test*. https://www.fda.gov/media/136282/download (accessed 2024-08-16).

(25) Matsumura, Y.; Shimizu, T.; Noguchi, T.; Nakano, S.; Yamamoto, M.; Nagao, M. Comparison of 12 Molecular Detection Assays for Severe Acute Respiratory Syndrome Coronavirus 2 (SARS-CoV-2). *Journal of Molecular Diagnostics* **2021**, *23* (2), 164–170. https://doi.org/10.1016/j.jmoldx.2020.11.007.

(26) Bioperfectus, J. *QuantStudio 5 real-time PCR system SARS-CoV-2 test*. http://www.bioperfectus.com/ (accessed 2024-08-16).

(27) Bio RAD. *Analytical sensitivity for samples with SARS-CoV-2, Flu A, and Flu B*. https://www.bio-rad.com/en-us/life-science-research/overlay/analytical-sensitivity-lod?ID=Analytical_1610048637 (accessed 2024-08-16).